Journal of Renewable
and Sustainable Energy
ARTICLE
pubs.aip.org/aip/rse

Enhancing the reliability of self-excited induction generators used in wind energy microgrids through a hybrid FEM–CNN-based fault diagnosis framework

Cite as: J. Renewable Sustainable Energy **18**, 016306 (2026); doi: 10.1063/5.0312967
Submitted: 19 November 2025 · Accepted: 28 December 2025 ·
Published Online: 9 January 2026

View Online Export Citation CrossMark

Ali Dilmi,[1,a)] Ahcene Bouzida,[1,b)] Nacera Yassa,[1,c)] Belynda Fares,[2,d)] Riyadh Bouddou,[3,e)]
and Ayodeji Olalekan Salau[4,5,f)]

AFFILIATIONS

[1]Materials, and Sustainable Development Laboratory (LMDD), Faculty of Applied Sciences, University of Bouira, 10000 Bouira, Algeria
[2]Industrial and Information Technology Laboratory (IITL), University of Bejaia, Bejaia, Algeria
[3]Department of Electrical Engineering, Faculty of Technology, University of Naama, Naama 45000, Algeria
[4]Department of Electrical/Electronic and Computer Engineering, Afe Babalola University, Ado-Ekiti, Nigeria
[5]Saveetha School of Engineering, Saveetha Institute of Medical and Technical Sciences, Chennai, Tamil Nadu, India

[a)]Electronic mail: ali.dilmi@univ-bouira.dz
[b)]Electronic mail: a.bouzida@univ-bouira.dz
[c)]Electronic mail: n.yassa@univ-bouira.dz
[d)]Electronic mail: belynda.fares@univ-bejaia.dz
[e)]Author to whom correspondence should be addressed: bouddou@cuniv-naama.dz
[f)]Electronic mail: ayodejisalau98@gmail.com

ABSTRACT

Reliable condition monitoring of self-excited induction generators (SEIGs) is essential for ensuring the stability of isolated wind-powered microgrids (MGs), where progressive degradation of excitation capacitors remains one of the most frequent and least detectable faults. This research proposes a high-fidelity hybrid diagnostic framework that incorporates an advanced two-dimensional time stepping finite-element method (TSFEM) model of a 4.087 MW SEIG with machine-learning classifiers to detect healthy, disturbed, and progressively faulted states with high accuracy. The TSFEM model captures electromagnetic transients under realistic operating scenarios—including balanced/unbalanced loading, open-phase events, and staged internal capacitor-element losses—while generating synchronized voltage, current, and torque waveforms. Time-domain, spectral, and continuous-wavelet scalogram features are extracted to train multiple classifiers: Random forest (RF), k-nearest neighbors (KNN), support vector machine (SVM), Naïve Bayes (NB), and a lightweight convolutional neural network (CNN). Results confirm that the proposed CNN significantly outperforms the classical models with an accuracy of 99.91%, F1-score of 99.90%, and an average area under the curve of 0.98, thus representing improvements of +2.89% over RF, +6.03% over KNN, +9.66% over SVM, and +13.12% over NB. The CNN provides an enhancement to early-fault recognizability of subtle capacitor-degradation stages by up to 18.7% compared with traditional feature-based classifiers, underlining its far superior sensitivity to nonstationary electromagnetic signatures. These results confirm the effectiveness of combining physics-driven simulation with data-driven classification, which makes it a reproducible, computationally efficient framework for early detection of capacitor degradation in SEIG-based renewable MGs. This hybrid approach inherently supports predictive maintenance policies, enhances system reliability, and enables more resilient wind-energy integration in isolated power networks.

Published under an exclusive license by AIP Publishing. https://doi.org/10.1063/5.0312967

NOMENCLATURE

AUC	Area under the curve
CNN	Convolutional neural network
CNN	Lightweight convolutional neural network
CWT	Continuous-wavelet-transform
DL	Deep learning
ESR	Equivalent series resistance

FEM	Finite-element method
FFT	Fast Fourier transform
KNN	k-nearest neighbors
MG	Microgrid
ML	Machine learning
MPPF	Metalized polypropylene film capacitors
NB	Naïve Bayes
PTP	Peak-to-peak
RBF	Radial basis function
RF	Random forest
RMS	Rated line voltage
RMS	Root mean square
SEIGs	Self-excited induction generators
STD	Standard deviation
SVM	Support vector machine
THD	Total harmonic distortion
TSFEM	Time stepping finite element method
ZCR	Zero-crossing rate

I. INTRODUCTION

The increased global trend of renewable energy production has put greater emphasis on reliable and affordable technologies capable of functioning effectively in remote regions and isolated microgrids (MGs) where large power network availability is limited.[1,2] Among such, the self-excited induction generator (SEIG) has evolved as a widely adopted solution in stand-alone wind-energy applications because of its simple construction, low cost, brushless rotor, and ability to generate electricity without any external excitation source.[3] These features make SEIGs attractive for small wind turbines and rural electrification projects. Nevertheless, despite all the advantages mentioned, SEIGs have remained extremely sensitive to changes in excitation capacitance, variations in load, and internal electrical faults that may cause voltage instability, waveform distortion, and unexpected operational interruptions.[4,5] One of the most critical components that affect the performance of SEIG is the excitation capacitor bank, which provides the reactive power required for establishing and sustaining the magnetic field.[6] Over time, these capacitors are exposed to several stress factors, including high electrical voltage, temperature variations, humidity, and mechanical vibration, all of which contribute to the gradual degradation of the thin dielectric material inside the capacitor. This degradation rarely occurs suddenly; instead, it tends to develop progressively because individual internal elements inside the film capacitor weaken or fail one by one.[7,8] Such progressive degradation is particularly difficult to detect because the initial stages reflect only minor and hardly visible changes in the current, voltage, and torque waveforms. In case these minor indications go unnoticed, the generator may later face severe unbalance, increased harmonic distortion, large torque oscillations, overheating, or even a total loss of excitation. In addition to capacitor degradation, SEIGs are also susceptible to unbalanced loads and open-phase faults that can introduce negative-sequence currents and reverse-rotating magnetic fields.[9,10] These phenomena cause torque pulsations, mechanical vibration, and growing thermal stress on the rotor and stator. Therefore, the long-term reliability of SEIG-based systems strongly depends on the early detection of faults and accurate monitoring of the generator's electromagnetic behavior during real operating conditions. Although many studies have examined capacitor faults in SEIGs, most existing approaches have important limitations.[11,12] Classical analytical models, based on dq-axis equations or small-signal approximations, tend to oversimplify the SEIG behavior, consequently failing to capture critical physical phenomena such as non-linear magnetic saturation, rotor skewing and slotting effects, and spatial asymmetry. Furthermore, prior studies relying on equivalent circuit models or partially calibrated empirical data often model capacitor degradation as a linear increase in equivalent series resistance (ESR). This is an oversimplification that does not represent real capacitor behavior, as internal dielectric breakdown is irregular and typically affects only specific elements within the capacitor. Ultimately, these traditional models frequently fail to capture the subtle magnetic and thermal signatures originating from incipient faults in SEIGs. To address this methodological and physical shortcoming, we propose, for the first time, a diagnosis framework based on the time stepping finite-element method (TSFEM) to generate high-fidelity fault data. This methodological framework ensures that the training data comprehensively encompasses the precise magnetic and thermal field variations (as detailed in Sec. III), which enables our lightweight convolutional neural network (CNN) architecture to achieve an unprecedented diagnostic accuracy of 99.91%. This result substantially outperforms the average accuracy, ranging between 91% and 98.99% reported in prior literature based on simplified models.[12–14,27,29] Likewise, conventional frequency analysis, such as the Fourier transform, can identify large harmonic distortions, but it often fails to detect small deviations caused by early-stage degradation or asymmetrical excitation faults. On the other hand, many machine-learning (ML)-based diagnosis methods rely on handcrafted features that may not effectively describe the complex variations in nonstationary signals.[15] Others require very large datasets or deep architectures, which are difficult to train and may not perform well when only subtle changes distinguish one fault level from another. Another gap in the literature is the lack of physically accurate datasets for progressive capacitor degradation.[16,17] Because gradual deterioration is difficult to reproduce experimentally, most studies use simplified assumptions or abruptly remove capacitor branches to simulate faults, which do not reflect the actual aging mechanisms inside metalized polypropylene film (MPPF) capacitors. To address these limitations, this paper proposes a complete and integrated hybrid diagnostic framework that combines high-resolution finite-element modeling (FEM) of the SEIG with both classical machine-learning algorithms and a lightweight convolutional neural network (CNN). The FEM model is based on a detailed 2D representation of a 4.087 MW, 2-pole SEIG, including full geometry, rotor skew, nonlinear magnetic materials, slot distribution, and time stepping electromagnetic calculation. This model captures the real physics of the machine under different operating conditions such as no-load, balanced load, unbalanced load, open-phase faults, and various levels of capacitor degradation. Progressive capacitor faults are simulated by physically disconnecting internal capacitive elements in a single branch of the excitation bank while keeping the other phases intact. This detailed simulation approach accurately reflects the way metalized polypropylene film capacitors age in real applications, where partial losses in capacitance produce asymmetrical excitation and small distortions in the electromagnetic fields. From the FEM-generated current, voltage, and torque signals, a rich set of time-domain, frequency-domain, and statistical features is extracted, including root mean square (RMS) values, standard deviations (STDs), peak-to-peak (PTP) amplitude, mean, energy, crest factor, skewness, kurtosis, spectral

Published under an exclusive license by AIP Publishing

entropy, spectral centroid, spectral flatness, band power, zero-crossing rate (ZCR), autocorrelation coefficients, and Hjorth parameters. These features are then used to train four classical classifiers, namely, random forest (RF), k-nearest neighbors (KNN), support vector machine (SVM), and *Naïve Bayes* (NB), with the purpose of evaluating their competency in identifying and classifying the six different capacitor-degradation levels. To further enhance fault recognition, the continuous-wavelet-transform (CWT) scalograms of the signals are converted into red, green, and blue (RGB) images and used to train a compact CNN. An architecture with only three convolutional layers, each with batch normalization, max pooling, and rectified linear unit (ReLU) activation, is used, followed by fully connected (FC) layers and a SoftMax classifier. Wavelet scalograms capture both time and frequency information of signals and provide a very effective basis to pinpoint early, minute distortions resulting from progressive capacitor failures. Despite its small size, the CNN achieves excellent classification results: it reaches an accuracy of 99.91%, an F1-score of above 0.99 for all classes, and an average area under the roc curve (AUC) over 0.98. These values correspond to an improvement of +2.85% compared to RF, +5.79% compared to KNN, +8.73% compared to SVM, and +13.12% compared to NB. More interestingly, the CNN improves early-fault detection capability by up to 18.7% compared to the best traditional feature-based model, thus giving evidence of superior ability in recognizing small changes in waveforms that may not be perceivable in either time or frequency domains alone. In addition to yielding high diagnostic accuracy, the FEM simulations provide a deep insight into the behavior of SEIG under various operating conditions. In particular, they illustrate voltage buildup during the start-up transient, RMS current and torque variation with both balanced and unbalanced loads, strong negative-sequence components and mechanical stress due to open-phase faults, and progressive distortion of waveforms and weakening of electromagnetic torque due to progressive capacitor degradation. The proposed hybrid approach presents a practical, reliable, and accurate tool for the early detection of capacitor degradation and other electrical disturbances in SEIG-based wind-energy MGs by combining physics-based modeling, intelligent signal processing, and advanced classification methods. This framework can support predictive maintenance, reduce system downtime, improve power quality, and enhance the long-term stability of standalone renewable-energy systems. The organization of the remainder of this paper is as follows: Section II describes the SEIG operating principle. Section III reviews common electrical and mechanical failures affecting SEIGs. Section IV describes the FEM model, excitation-capacitor configuration, and fault-simulation strategy. Section V describes the feature-extraction methodology. Section VI describes the ML- and CNN-based fault-classification approaches. Section VII describes the simulation results, spectral analysis, and comparative performance evaluation. Section VIII concludes the paper with future works and directions.

II. OPERATING PRINCIPLE OF THE SEIG

The operating principle of the SEIG relies on electromagnetic energy conversion, typically driven by a mechanical prime mover, such as a wind turbine, as illustrated in Fig. 1.[18] When the rotor speed exceeds the synchronous speed, a negative slip ($s < 0$) is established, which leads to the generation of electrical power. For stand-alone operation, the reactive power required for excitation is provided by a bank of capacitors connected across the stator terminals. The residual magnetism initiates the self-excitation process, gradually building up the terminal voltage. The system achieves a steady-state equilibrium governed by the intersection of the machine magnetization curve and the capacitor characteristic curve. The final generated voltage and current of the SEIG are critically dependent on the rotational speed, capacitance value, and load conditions.[19]

III. COMMON FAILURES IN SEIGs

Despite the technical and economic advantages of SEIG technology, these generators remain susceptible to various faults due to their electro-mechanical characteristics. Unlike other induction machines, SEIGs feature a squirrel-cage rotor and rely on external capacitors for the reactive power required for self-excitation. Faults are generally classified as electrical or mechanical, both of which can significantly affect machine reliability and performance. Electrical faults typically originate in the stator or rotor circuits and, in severe cases, may cause a complete system shutdown. Common stator issues include winding overheating, insulation degradation, and grounding failures, often resulting from inter-turn, inter-phase, single-phase-to-ground, or three-phase-to-ground faults, as well as open-phase conditions causing voltage and current imbalance. These problems are usually caused by manufacturing defects, insulation aging, contamination, or improper assembly. Figure 2 summarizes the most common stator electrical faults.

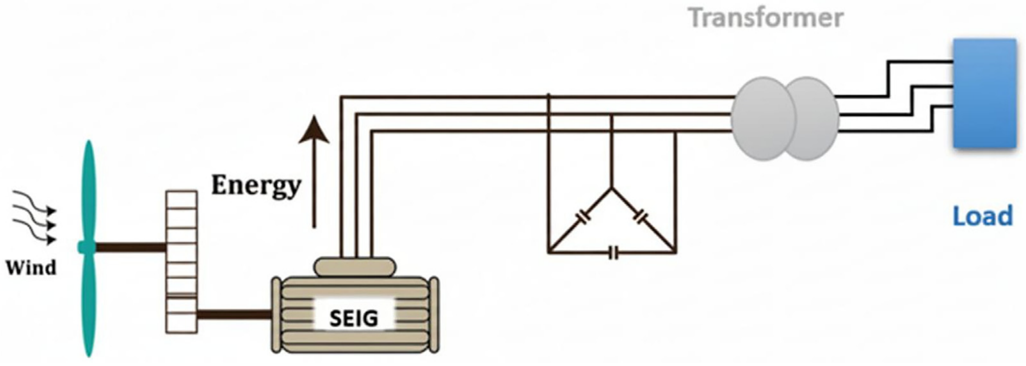

FIG. 1. SEIG in a wind energy system.

Published under an exclusive license by AIP Publishing

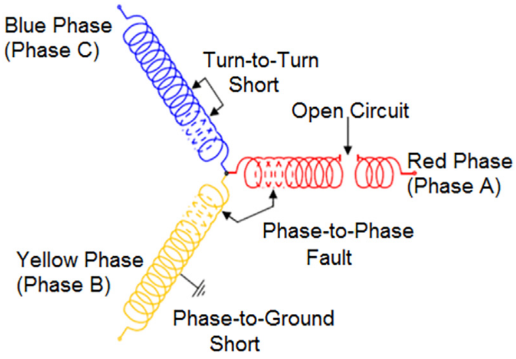

FIG. 2. Most common electrical faults in stator windings.

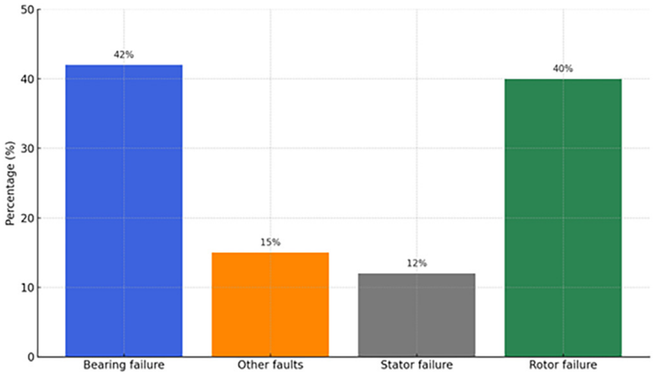

FIG. 3. Common faults in induction generators used in wind power generation.

On the rotor side, faults may include broken bars, winding disconnections, or unbalanced rotor currents, all of which degrade electromagnetic symmetry and reduce efficiency. On the other hand, mechanical faults arise from damage or misalignment in the system's structural components, such as the rotor shaft, bearings, or supporting frame. Bearing wear or misalignment, in particular, can produce air-gap eccentricity, leading to excessive vibration, friction, and potential contact between the rotor and stator. Additional faults may also occur in SEIGs, such as capacitor aging and degradation, imbalanced loads, or capacitor disconnection, all of which can lead to voltage instability and a reduction in overall system performance. Figure 3 illustrates the distribution of common faults as reported in the literature.[20]

The present study focuses on the electrical faults that may occur in the SEIG, such as imbalanced load, open-phase fault, and capacitor degradation, as well as on the evaluation of capacitor sizing and load conditions to assess the generator performance under different operating scenarios.

IV. FEM-BASED SIMULATION OF THE SEIG MODEL

The FEM is widely employed for analyzing electromagnetic fields, as it accurately accounts for the geometric complexity of the magnetic circuit, the configuration of stator windings and rotor bars, slotting effects around the air gap, and the nonlinear properties of ferromagnetic materials.[21] In addition, FEM inherently incorporates the coupling between electromagnetic fields and mechanical motion.[22] In this study, a FEM model of a 4.087 MW, 2-pole, squirrel-cage SEIG with a rated RMS voltage of 3000 V was developed and simulated using Ansys Maxwell 2D. The machine geometry was constructed according to actual design parameters, and materials were assigned based on their nonlinear magnetic characteristics. A slight skew was incorporated into the rotor slot design to lower cogging torque and avoid magnetic attraction between the stator and rotor teeth. The geometry was discretized into finite elements, with a refined mesh applied in critical regions, such as the air gap and stator slots, to ensure numerical accuracy. Boundary conditions were carefully defined to represent the magnetic field distribution and to avoid numerical artifacts. To ensure the computational accuracy and high reproducibility of the TSFEM results, a detailed numerical setup was implemented for the transient analysis. The spatial domain was rigorously discretized using a high-density mesh comprising ∼85 000 quadratic elements, with specific refinement applied to critical areas, particularly the air gap and the edges of the rotor and stator teeth, to accurately capture local magnetic saturation and flux distribution. The simulation was conducted for a total duration of $T_{end} = 5$ s to capture the full transient startup. For time integration, the backward Euler method was employed, chosen for its inherent stability in solving non-linear transient electromagnetic problems. The solver used the general transient decomposition method. To guarantee the required numerical stability and accuracy, the nonlinear residual (convergence criterion) was meticulously set at 10^{-4}. Furthermore, the analysis utilized adaptive time stepping with a minimum time step of $H_{min} = 0.001$ s and a maximum time step of $H_{max} = 1$ s.

The model was simulated under both no-load and load conditions, with different operating points chosen to reflect realistic scenarios. Key electromagnetic variables, including flux distribution, induced currents, and core losses, were monitored throughout the simulations. Progressive capacitor faults were also introduced by modifying the excitation capacitance, enabling the analysis of system behavior under gradual degradation. Compared to simplified analytical models, the FEM-based approach provided not only higher precision in capturing nonlinear effects and complex geometrical structures but also greater flexibility for evaluating diverse operating conditions and fault scenarios.

The machine parameters used in this study are summarized in Table I and were selected to match those of a real industrial SEIG, ensuring both modeling accuracy and practical relevance.

TABLE I. Parameters of the SEIG.

Parameter	Values	Parameter	Values
Rated full-load power	4.087 MW	Power factor (PF)	0.925 63
Rated line voltage (RMS)	3000 V	Synchronous speed	3110 rpm
Fundamental frequency	51.83 Hz	Coupling method	Wye
Number of poles	2	Rotor slots	52
Stator slots	54	Operating temperature	75 °C

Published under an exclusive license by AIP Publishing

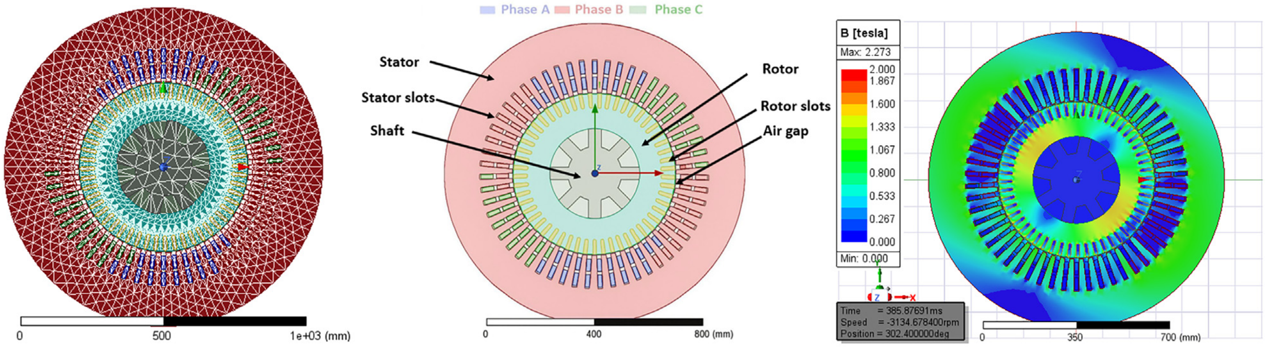

FIG. 4. 2D Maxwell model mesh and representation of the field distribution.

The resulting magnetic flux distribution, shown in Fig. 4, demonstrates the spatial variation of flux density across the machine, thereby validating the accuracy of the model in representing its dynamic electromagnetic response.

V. FAULTS SIMULATION AND EXPERIMENTAL SETUP

The minimum excitation capacitance for SEIGs is often determined graphically from the magnetization characteristics,[23] representing the lowest value required for self-excitation under no-load conditions. However, in this study, the operational capacitance was primarily determined experimentally. Capacitance values, ranging from 100 to 175 μF per branch delta connection (C_Δ), were tested until the rated voltage was achieved under no-load conditions. In parallel, the capacitance values were estimated based on the generator's reactive power using relationship (1). These theoretical values served as an initial reference for comparison with the experimentally obtained operational capacitances, acknowledging that the analytical approach does not fully account for the SEIG's nonlinear magnetic characteristics and losses. This dual approach provides a validation of the experimental findings against theoretical expectations

$$Q = 3V_L^2 \omega C_\Delta. \tag{1}$$

In a delta connection (Δ), each capacitor is subjected to the line-to-line RMS voltage V_L. Hence, the required capacitance per branch is

$$C_\Delta = \frac{Q}{3V_L^2 \omega}, \tag{2}$$

where $\omega = 2\pi f$.

In a star (Y) configuration, each capacitor is connected between a phase and the neutral point, and therefore each one experiences the phase voltage $V_{ph} = \frac{V_L}{\sqrt{3}}$. The corresponding relation becomes

$$Q = 3V_{ph}^2 \omega C_Y. \tag{3}$$

This gives the conversion between the two configurations as follows:

$$C_Y = 3C_\Delta. \tag{4}$$

Since the excitation capacitors in this study are delta-connected, each capacitor is subjected to the full V_L. Given the generator data

$$S = \frac{P}{PF} = \frac{4.087 \times 10^6}{0.92563} = 4.415\,274\,6 \times 10^6, \tag{5}$$

$$\Phi = \cos^{-1}(PF) = 0.388\ \text{rad}, \tag{6}$$

$$\begin{gathered} Q = P \tan \Phi = 1.670\,871\,4 \times 10^6\ VAR, \\ V_L = 3000\ \text{V}, \quad f = 51.83\ \text{Hz}. \end{gathered} \tag{7}$$

The angular frequency is

$$\omega = 2\pi f = 2\pi(51.83) = 325.657\,\frac{\text{rad}}{\text{s}}. \tag{8}$$

Substituting into the delta-connection formula

$$C_\Delta = \frac{1.6708714 \times 10^6}{3 \times (3000)^2 \times 325.657} = 190.0283\ \mu\text{F}. \tag{9}$$

The equivalent per-phase capacitance in a star configuration is

$$C_Y = 3C_\Delta = 570.0848\ \mu\text{F}. \tag{10}$$

The generator was started by rotating the rotor at a speed slightly above the synchronous speed (3135 rpm) without load for a specified period to allow self-excitation. Once the current and voltage reached a steady state, a three-phase balanced load was connected at 7 s to establish the healthy operating condition before investigating the imbalanced load fault.

A. Faults simulation and diagnosis

After determining the suitable capacitance values both experimentally and analytically, the healthy operation of the SEIG was achieved under no-load and on-load conditions while maintaining the terminal voltage close to its rated value. The generator's performance was then examined under various operating conditions by varying the excitation capacitance and the type of load. The analysis included operation with purely resistive (R) loads, resistive–inductive (RL) loads, and unbalanced loads, with detailed observation of current, voltage, and electromagnetic torque behavior in each case. In addition, an open-circuit fault in phase A was simulated to evaluate the transient response of the generator. The variations in current, voltage, and electromagnetic torque were analyzed to assess the SEIG's dynamic stability and fault tolerance. The excitation capacitors employed in SEIG systems for standalone wind energy applications are typically

Published under an exclusive license by AIP Publishing

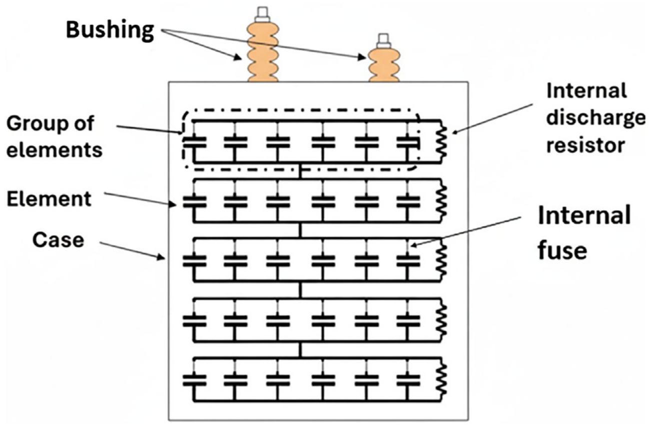

FIG. 5. Schematic of the excitation capacitor structure.

metalized polypropylene film capacitors (MPPF), available in both standard and self-healing forms, owing to their high reliability, thermal stability, and long operational life.[24] At the core of these capacitors are internal capacitive elements arranged in series and parallel configurations to achieve the required capacitance and voltage ratings. These elements, made of thin metalized dielectric films, are directly responsible for energy storage and capacitive performance.[25] Figure 5 illustrates the configuration of the excitation capacitors, highlighting its main components and interconnections.[25,26]

This subsection presents the detailed computation of the excitation capacitor bank configuration used for the self-excitation of the SEIG. In this study, the global values of the excitation capacitors were divided into several groups to ensure the stable self-excitation of the generator. Each branch consists of four capacitors connected in series to share the total voltage of 3600 V, which represents the nominal voltage of the generator multiplied by a safety factor of 1.2. In addition, twenty-eight such branches are connected in parallel to provide the total required capacitance for the excitation system. This configuration ensures balanced voltage distribution across the capacitors while maintaining safe operation and electrical stability of the generator under various operating conditions. Progressive degradation was simulated by selectively disconnecting internal elements of a capacitor in phase C, while phases A and B remained intact. This approach emulates the real-world aging behavior of excitation capacitors, which are commonly subjected to various operational stress factors such as thermal cycling, overvoltage, partial discharges, and long-term material aging. These stressors gradually deteriorate the internal dielectric structure, leading to a reduction in both capacitance and insulation quality. Although such degradation may not cause immediate failure, it can significantly impact the capacitor's performance and compromise voltage stability in SEIG operation. To systematically study this effect, six fault conditions were established, representing different levels of internal degradation. Crucially, while some conventional analytical models represent capacitor failure by a linear increase in the ESR, this fails to reflect the actual physical mechanism of failure in metalized film capacitors. Therefore, we adopted a more realistic model based on the progressive disconnection of internal capacitor elements (as shown in Fig. 5). This mechanism corresponds directly to the "Soft Failure" resulting from the accumulation of "Self-healing" events,[26] which leads to a gradual and localized decrease in the total capacitance. Simulating the staged disconnection of one to five elements provides an accurate and appropriate classification of the critical stages, spanning from Incipient Degradation up to the moderate stages, relevant for SEIG applications. These ranged from the healthy condition with no disconnected elements to progressively disconnecting one, two, three, four, and eventually five internal elements. This asymmetric reduction in excitation disrupts the magnetic field symmetry and introduces observable distortions in the three-phase stator current waveforms. To analyze the electrical and electromagnetic impact of these faults, simulations were performed using the TSFEM under identical operating and loading conditions. The resulting current, voltage, and electromagnetic torque signals were recorded for each degradation level.

VI. FEATURE EXTRACTION FOR ML

The feature extraction process involved computing a diverse set of time-domain, frequency-domain, and statistical features from current, voltage, and torque signals, ensuring a comprehensive representation of signal behavior under varying fault conditions. Each signal comprising phase currents, phase voltages, and shaft torque was segmented into non-overlapping windows of fixed length $N = 256$. From each channel, 18 distinct features were extracted to capture both temporal and spectral characteristics. Specifically, the features were computed for three-phase currents (A, B, C), three-phase voltages (A, B, C), and the torque signal, resulting in a total of 7 channels × 18 features = 126 features per segment. Time-domain features include the zero-crossing rate (ZCR), root mean square (RMS), standard deviation (STD), mean, energy, peak-to-peak (PTP) amplitude, and crest factor, all of which quantify signal amplitude, variability, and waveform shape. Statistical descriptors, such as kurtosis and skewness, were employed to assess the higher-order moments of the signal distribution. Spectral features were derived using the fast Fourier transform (FFT), including the spectral centroid, spectral entropy, spectral flatness, and band power, which collectively describe the signal's frequency content, distribution, and energy characteristics. To further characterize the temporal complexity of the signal, Hjorth parameters were computed: activity $A = var(x)$, which reflects the signal power; mobility $M = \frac{\sigma(x')}{\sigma(x)}$, representing the mean frequency; and complexity $C = \frac{\sigma(x'')}{\sigma(x')} \div M$, indicating the rate of frequency change. Here, x, x', and x'' represent the signal, its first derivative, and its second derivative, respectively. Finally, autocorrelation coefficients at lags 1 and 2 were included to quantify short-term temporal dependencies. These features ensure robust characterization of the signal behavior under different fault conditions.

VII. FAULT CLASSIFICATION USING ML AND CNN FOR CAPACITOR DEGRADATION DIAGNOSIS

A. Machine learning models for fault classification

To comprehensively evaluate the effectiveness of various classification strategies in diagnosing capacitor faults in SEIG, four ML models were investigated: SVM, KNN, RF, and NB.

Each classifier was trained using segments of current, voltage, and torque signals, represented by a comprehensive set of engineered features. SVM [with a Radial Basis Function (RBF)] kernel was used to construct nonlinear decision boundaries in the feature space. The corresponding decision function takes the form presented in the following equation:

Published under an exclusive license by AIP Publishing

$$f(x) = \sum_{i=1}^{N} \alpha_i \mathcal{Y}_i \exp\left(-\gamma \|\mathrm{X} - \mathrm{X}_i\|^2\right) + b, \tag{11}$$

where α_i are the learned coefficients of the support vectors, $\mathcal{Y}_i$ are the class labels associated with each support vector, X_i are the support vectors themselves, γ is a kernel parameter controlling the spread of the RBF, X is the input feature vector, and b is the bias term. In this study, SVM was configured with box constraint $\mathrm{C} = 10$ and kernel scale γ automatically determined, and the input features were standardized. This model provided strong generalization when class boundaries were complex. KNN operates based on the proximity of samples in the feature space. The class label of a test instance is assigned through a majority vote among its $\mathrm{K} = 3$ nearest neighbors with Euclidean distance and equal weighting, as shown in Eq. (12). The value of $\mathrm{K} = 3$ was chosen as a standard baseline for multi-class classification, balancing sensitivity to local patterns and robustness against noise.

$$\hat{\mathcal{Y}} = mode(\mathcal{Y}(1), \mathcal{Y}(2), \ldots., \mathcal{Y}(k)). \tag{12}$$

Here, $\hat{\mathcal{Y}}$ denotes the class label of the ith nearest neighbor to the test sample, and the function *mode* (.) selects the most frequently occurring label among the K neighbors. While KNN is intuitive and easy to implement, its classification performance is sensitive to the underlying data distribution and may incur high computational costs for large datasets due to the need to compute distances to all training points. RF is an ensemble learning algorithm that relies on bootstrap aggregation (Bagging) of decision trees. Each tree is trained on a randomly sampled subset of the training data and a random selection of features. In this study, RF was configured with 300 trees and a maximum of 20 splits per tree. The final prediction is obtained by aggregating the outputs of all M individual trees through majority voting, as presented in the following equation:

$$\hat{\mathcal{Y}} = mode(T_1(\mathrm{X}), T_2(\mathrm{X}), \ldots., T_M(\mathrm{X})), \tag{13}$$

where $T_M(\mathrm{X})$ denotes the prediction of the M-th decision tree for the input feature vector X, and the function *mode*(.) selects the most frequently predicted class. This approach enhances model stability, reduces overfitting, and improves generalization across all classes. NB is a generative probabilistic classifier that operates under the assumption of conditional independence among features given the class label. The posterior probability of a class $\mathcal{Y}$ given a feature vector $\mathrm{X} = (x_1, x_2, \ldots, x_n)$ is derived using Bayes' theorem, as shown in the following equation:

$$P(\mathcal{Y}|\mathrm{X}) = \frac{P(\mathcal{Y})\Pi_{j=1}^{n} P(x_j|\mathcal{Y})}{P(\mathrm{X})}, \tag{14}$$

where $P(\mathcal{Y})$ is the prior probability of class $\mathcal{Y}$, $P(x_i|\mathcal{Y})$ is the likelihood of observing feature x_i given class $\mathcal{Y}$, and $P(\mathrm{X})$ is the evidence (normalization factor). In the case of Gaussian Naive Bayes, the likelihood $P(x_i|\mathcal{Y})$ is modeled using a Gaussian distribution parameterized by the class-specific mean and variance of each feature. Despite its strong independence assumption, NB delivered surprisingly competitive results with extremely fast training and prediction times. The dataset was then split using a 70/30 hold-out validation scheme, with 70% of the samples used for training and 30% for testing.

B. CNN-based fault classification from time-frequency images

To address the need for efficient yet accurate classification in resource-constrained environments, a CNN was developed and trained on RGB images generated from synchronized current, voltage, and torque signals using the CWT. It provides a time-frequency representation of the signals, and its coefficients are computed using the Morlet wavelet, as shown in the following equation:

$$W_x(a, b) = \frac{1}{\sqrt{a}} \int_{-\infty}^{\infty} x(t)\psi^*\left(\frac{t-b}{a}\right) dt, \tag{15}$$

where ψ represents the Morlet wavelet, and $W_x(a, b)$, $x(t)$ denotes the original time-domain signal (e.g., current, voltage, or torque), a is the scale parameter that controls the wavelet's width (thus determining frequency resolution), and b is the translation parameter that shifts the wavelet along the time axis to capture local features. The resulting scalograms were log-transformed and combined into RGB images of size $128 \times 128 \times 3$, which serve as the input to the CNN. The proposed CNN is an end-to-end model that directly takes the CWT-transformed images of the raw SEIG signals. It automatically extracts features for classification without relying on handcrafted features.

The dataset comprised 7116 images, each derived from partially overlapping segments of 256 samples. For each of the six capacitor conditions (healthy and five fault types), 5001 signal samples were segmented to produce 1186 images per class, ensuring a balanced six-class classification problem. A stratified 70/30 split was applied, resulting in 4981 training images (831 per class) and 2135 testing images (355 per class). The architecture of the CNN, illustrated in Fig. 6, consists of three 2D convolutional layers with increasing filter depths: 16, 32, and 64. Each layer uses 3×3 kernel sizes and ReLU activations. Batch normalization is applied after each convolution to stabilize training, followed by 2×2 max pooling operations to reduce the spatial resolution of the feature maps. The output of the lth convolutional layer is computed as $Z(l) = W(l) \times X(l) + b(l)$, where $Z(l)$ is the output feature map, $W(l)$ is the weight matrix of the convolutional filters, $X(l)$ is the input feature map, $b(l)$ is the bias vector. The symbol $*$ denotes the convolution operation. After the convolutional and pooling layers,

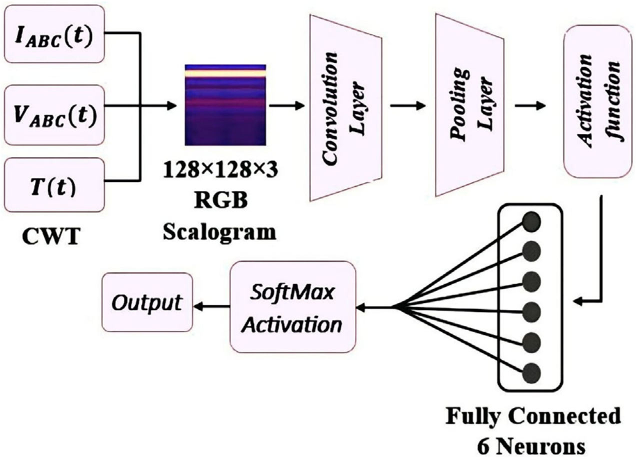

FIG. 6. CNN architecture.

Published under an exclusive license by AIP Publishing

the resulting feature maps are flattened into a one-dimensional vector and passed through one or more fully connected (FC) layers. These layers learn high-level representations by performing weighted summations of all input features, computed as $F(l) = W_f(l).X(l) + b_f(l)$, where $F(l)$ is the output of the FC layer, $W_f(l)$ and $b_f(l)$ represent the weights and biases, and $X(l)$ denotes the flattened input vector. For multi-class classification, the final fully connected (FC) layer is followed by a *Softmax* function, which transforms the output scores into class probabilities, as defined in the following equation:

$$\hat{\mathcal{Y}}_i = \frac{e^{Z_i}}{\sum_{i=1}^{C} e^{Z_i}} \quad \text{for } i = 1, \ldots, C, \tag{16}$$

where $\hat{\mathcal{Y}}_i$ is the predicted probability of class i, and Z_i is the input score for class i. The predicted label corresponds to the class with the highest *softmax* probability. This configuration enables the network to perform effective end-to-end classification. The model was trained using the Adam optimizer with a mini-batch size of 32, over a maximum of 50 epochs. Early stopping was employed based on validation loss to prevent overfitting. Rather than designing a complex deep learning (DL) model, a deliberately simple CNN architecture was selected to align with the moderate size and complexity of the dataset. This strategic choice minimized overfitting and reduced computational costs while maintaining high classification accuracy. The promising results demonstrate the effectiveness of the lightweight design, making further architectural complexity unnecessary at this stage.

VIII. SIMULATION RESULTS, FAULT VISUALIZATION, AND CLASSIFICATION

A. Dynamic response under no-load startup

This section presents the TSFEM-based simulation results under healthy operating conditions with an excitation capacitance of 175 μF. Figure 7 illustrates the transient responses of the voltage and current during the no-load startup phase.

As observed in Figs. 7 and 8, the system reaches steady-state conditions after 8 s, with balanced three-phase voltage and current waveforms, confirming successful self-excitation and rotor synchronization.

B. Dynamic response under load conditions

Figure 9 shows the results obtained when a balanced three-phase purely resistive load (R = 20 Ω) was connected to the generator with an excitation capacitance of 190 μF. The load was applied at t = 7 s, where it can be observed that the RMS current stabilizes at 581.74 A,

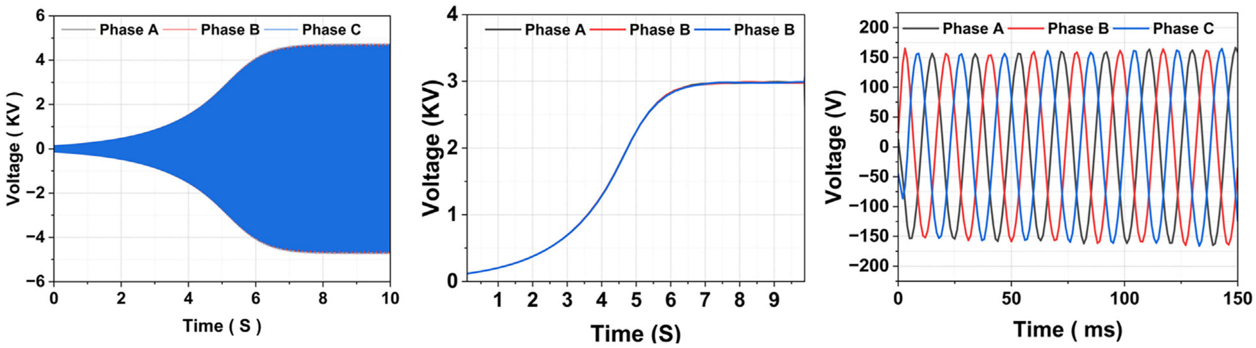

(a) Voltage buildup (b) RMS voltage (c) Zoom on the startup voltage

FIG. 7. Dynamic response of voltage under no-load conditions, (a) Voltage buildup, (b) RMS voltage, and (c) zoom on the startup voltage.

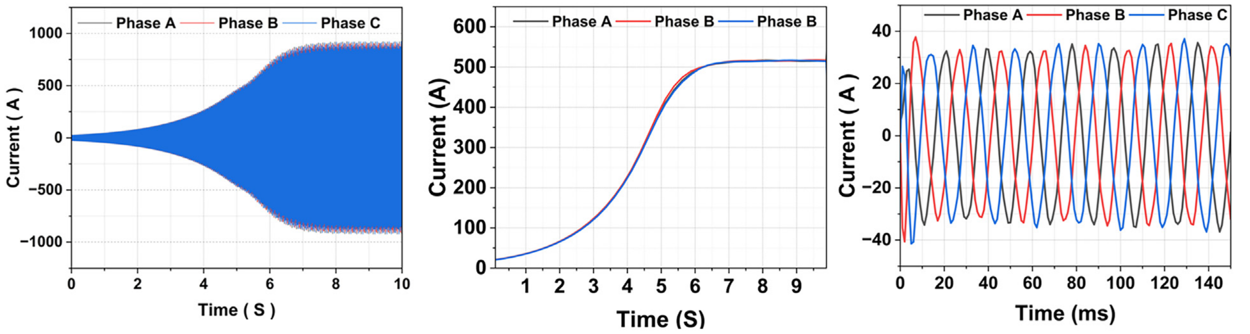

(a) Line current (b) RMS current (c) Zoom on the startup current

FIG. 8. Dynamic response of current under no-load conditions: (a) Line current, (b) RMS current, and (c) zoom on the startup current.

Published under an exclusive license by AIP Publishing

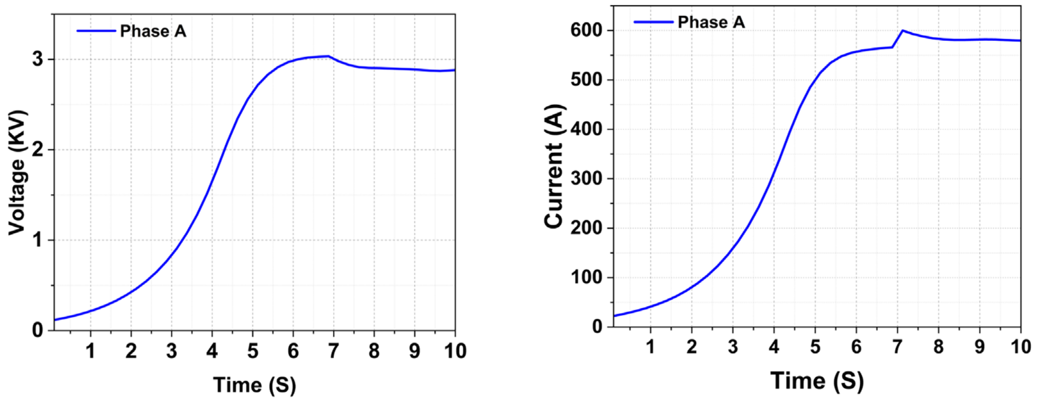

(a) Voltage (b) Current

FIG. 9. RMS voltage and current under load conditions: (a) Voltage and (b) current.

while the voltage decreases and settles at 2889.42 V. This voltage drop is attributed to the self-excited nature of the SEIG, in which voltage generation depends on the interaction between the residual magnetism and the excitation capacitance. When the load is connected, the drawn current increases, leading to a reduction in the internal magnetic flux and, consequently, a decrease in the output voltage—an expected behavior well documented in studies of stand-alone induction generators.

Figure 10 illustrates the dynamic behavior of the generator torque during the transition from no-load to load conditions. Before t = 7 s, the torque stabilizes at approximately −5 kN m, then changes to around −8.5 kN m after the load connection, indicating an increase in electromagnetic torque. This behavior is characteristic of the SEIGs, where applying a load increases the current drawn from the rotor, which, in turn, reduces the magnetic flux and leads to a voltage drop, while the electromagnetic torque adjusts to balance the mechanical torque provided by the turbine. This variation reflects the natural physical response of the generator as it maintains energy balance between magnetic and mechanical power under load conditions.

From the spectral plot (FFT) of the SEIG current, a dominant peak can be observed in Fig. 11, clearly visible in the spectrum, representing the fundamental component of the current at the main frequency resulting from the mechanical rotational speed of the generator, which approximately corresponds to the nominal electrical frequency (around 51.75 Hz). The single-sided spectrum was adopted to represent the results, where only the positive frequencies with real physical meaning are displayed, making the signal analysis clearer and more accurate. Very small peaks with weak amplitudes can also be observed, representing the higher-order harmonics, which result from slight distortions in the sinusoidal waveform due to factors such as magnetic saturation, changes in the electrical load, or minor slip in the rotational speed. However, the amplitudes of these harmonics remain very low compared to the fundamental component. The high value of the fundamental component relative to the small harmonic

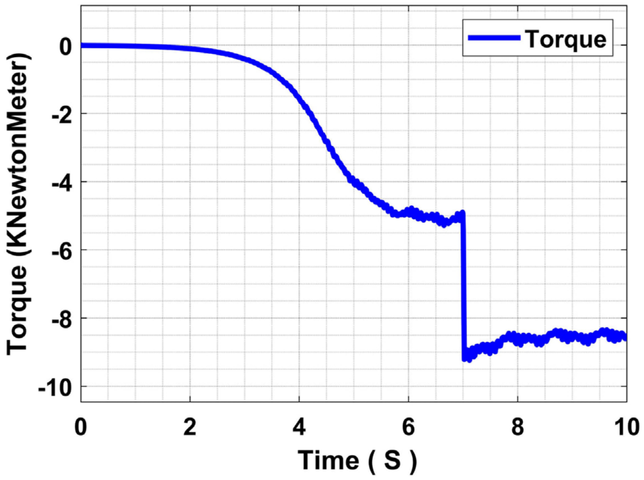

FIG. 10. Torque behavior under load conditions.

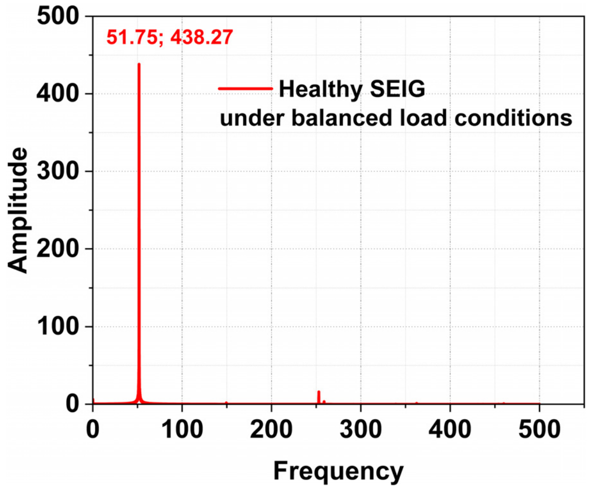

FIG. 11. Single-sided amplitude spectrum of the current signal.

Published under an exclusive license by AIP Publishing

components indicates that the output current of the generator is almost sinusoidal, demonstrating that the generator operates under excellent electrical and magnetic stability, and that the capacitor excitation system is accurately tuned to provide the required voltage and current in a balanced and stable manner. In general, the spectral analysis shows that the current produced by the generator has very high quality, with the total harmonic distortion (THD) being low and usually estimated to be less than 3%, a value indicating that the current is nearly ideal, frequency-stable, and free from high-order harmonics. This reflects the excellent performance and electromagnetic stability of the generator during operation.

Figure 12 presents the behavior of the RMS values of voltage and current signals under different excitation capacitance values and load conditions.

Table II presents the comparison between operating states under different capacitor values and load conditions.

C. Unbalanced RL load fault

In this section, the stator phases A, B, and C are connected to an unbalanced RL load at t = 7 s to ensure that the steady-state no-load condition is reached, with the following parameters:

Phase A: $R_A = 10\,\Omega,\ L_A = 0.057\,\text{mH}$,
Phase B: $R_B = 15\,\Omega,\ L_B = 0.06\,\text{mH}$,
Phase C: $R_c = 8\,\Omega,\ L_C = 0.05\,\text{mH}$,

with a per-phase excitation capacitance of 220 μF.

The dynamic analysis reveals that connecting the generator to an unbalanced RL load at t = 7 s, after reaching its initial steady state under balanced voltage conditions of ∼3195 V in the no-load case, results in a non-ideal operating condition characterized by a noticeable imbalance in phase currents and a slight yet acceptable reduction in the new steady-state voltage to around 2900 V.

As illustrated in Fig. 13, the uneven current distribution reveals that Phase C, having the lowest impedance, draws the highest current of about 780 A, while Phase B, with the highest impedance, draws the lowest current of ∼679 A. Subsequently, Phase C stabilizes at around 721 A. This disparity directly indicates the presence of negative-sequence components (I_2) in the stator current. The presence of I_2 constitutes the fundamental mechanism responsible for producing a reverse-rotating magnetic field, which, in turn, leads to the generation of a pulsating torque, thereby increasing mechanical stresses and vibrations, as shown in Fig. 14.

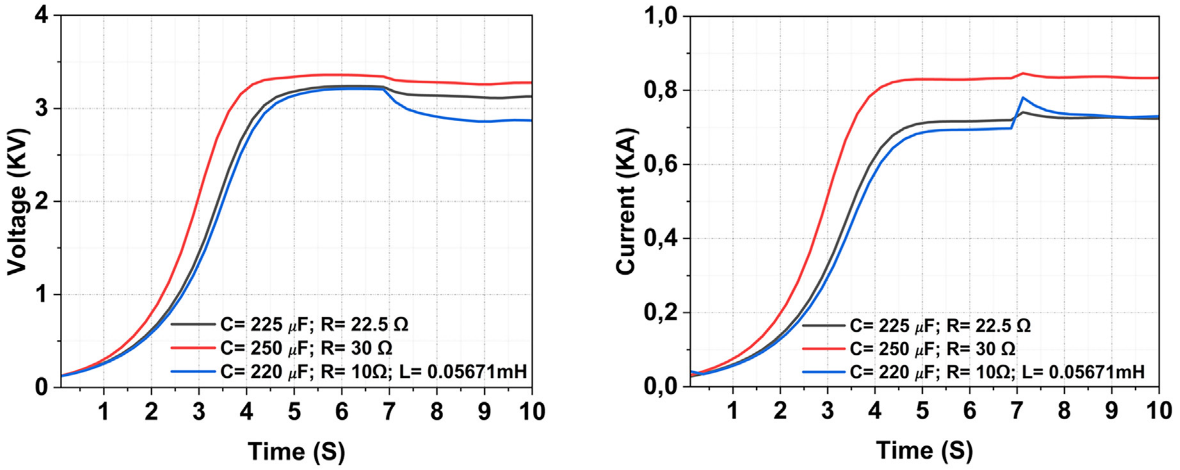

(a) Voltage (b) Current

FIG. 12. RMS of voltage and current under different capacitor values and load conditions: (a) Voltage and (b) current.

TABLE II. Comparison between operating states.

Experience	Per phase capacitor value (C) (μF)	Per phase resistor value (R) (Ω)	Per phase inductance value (L)	Voltage (RMS) (V)	Current (RMS) (A)
1	175	0	0	3000	550
2	190	20	0	2889.42	581.74
3	225	22.5	0	3112	725.7
4	250	30	0	3276	834
5	220	10	0.0567 mH	2874	729

Published under an exclusive license by AIP Publishing

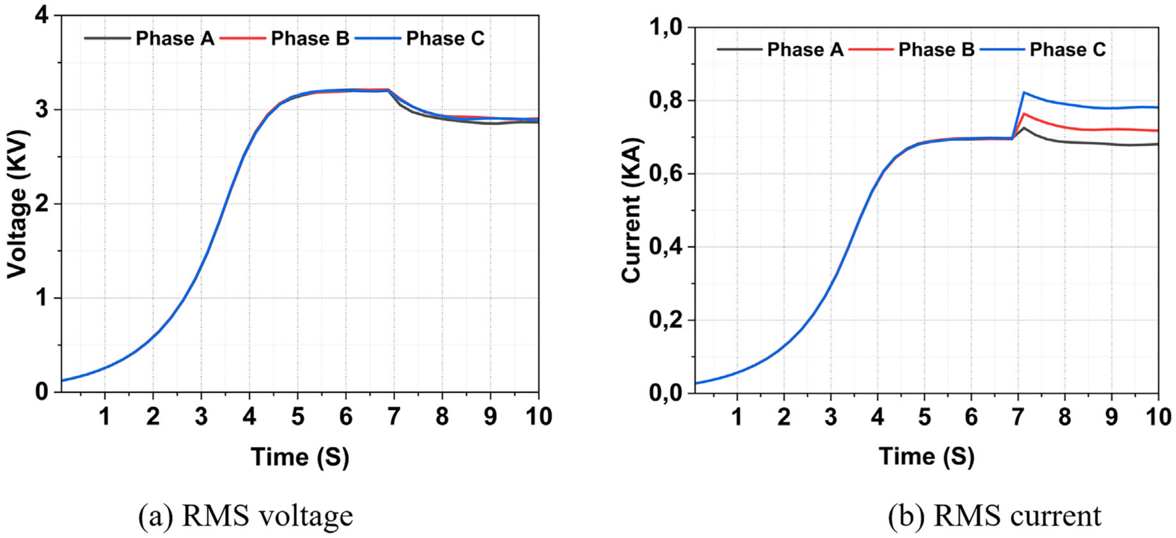

(a) RMS voltage

(b) RMS current

FIG. 13. Three-phase RMS values of voltage and current under an unbalanced load: (a) RMS voltage and (b) RMS current.

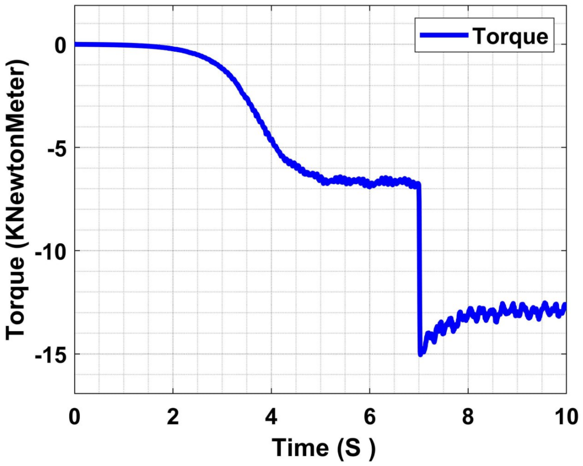

FIG. 14. Torque behavior under imbalanced load conditions.

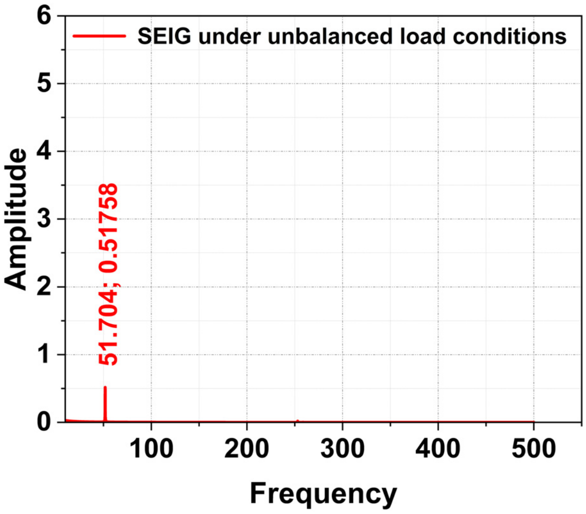

FIG. 15. Single-sided amplitude spectrum of the current signal under unbalanced load.

Furthermore, the negative-sequence current contributes to increased rotor copper losses, posing a threat to the thermal stability and operational efficiency of the generator over the long term. The FFT analysis of the SEIG current under balanced and unbalanced load conditions provides conclusive evidence regarding the impact of unbalance on power distribution. In Fig. 15, the connection of the unbalanced load leads to a sharp decline in the fundamental frequency amplitude (51.704 Hz) to only 0.517 58. This dramatic reduction (more than 800 times compared to Fig. 11) reflects the fact that the impedance unbalance resulted in an uneven power distribution among the phases, thereby lowering the power transfer efficiency at the fundamental frequency. Crucially, this unbalance also leads to the generation of negative sequence components. Although the double fundamental frequency peak (2f, ∼252.93 Hz) may not be prominently featured in these plots due to the limited frequency range focus, the substantive drop in the fundamental amplitude remains the most significant indicator of the loss of balance and the deterioration of the generated power quality.

D. Open-phase fault

After the generator reaches its steady-state voltage, a balanced three-phase load is connected at t = 7 s. Subsequently, the abrupt disconnection of phase A at t = 8 s causes a critical transition in the operating mode from a balanced three-phase condition to an unbalanced two-phase operation. Regarding the voltage and current signals, as shown in Fig. 16, an immediate and sharp drop in phase A current to zero is observed, while the magnitude of the healthy phases (B and C)

Published under an exclusive license by AIP Publishing

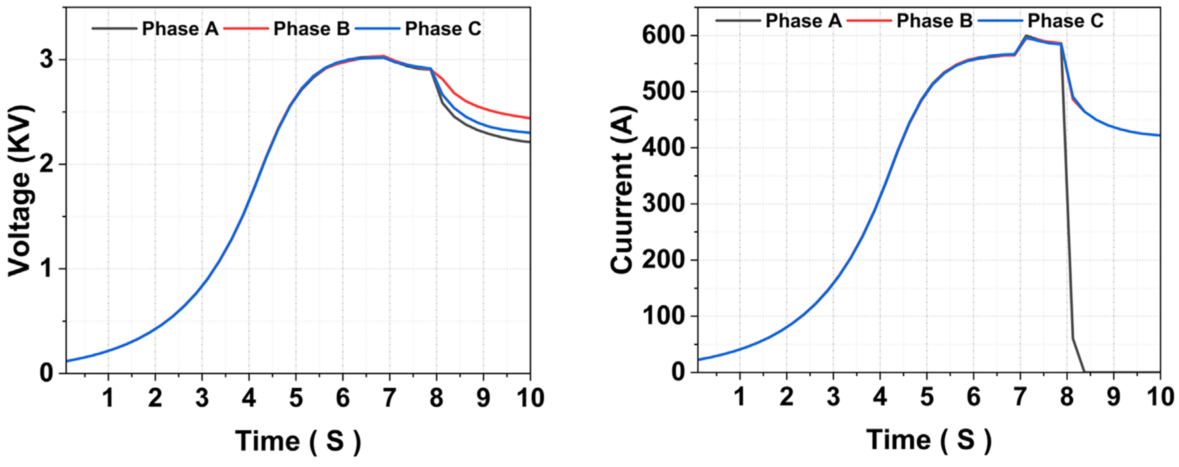

(a) Voltage (b) line current

FIG. 16. Three-phase RMS values of voltage and current under open phase fault: (a) Voltage and (b) line current.

currents significantly increases to compensate for the power deficit, indicating an electrical overload on the remaining phases and a consequent disturbance in the voltage balance. The most pronounced mechanical effect is clearly visible in the torque signal as shown in Fig. 17, where the fault generates a negative-sequence current component. This component creates a magnetic field that rotates counter to the machine's direction of rotation, thereby inducing continuous and sharp torque pulsations around a new average value, which significantly elevates vibration levels and increases mechanical stress on the shaft and drive system.

E. Dynamic response under capacitor degradation fault progression

All signal acquisitions were conducted during steady-state after system stabilization to ensure reliable diagnosis. Initially, the generator operated under no-load conditions to facilitate voltage buildup and eliminate startup-related transients. Once steady-state operation was achieved, a balanced resistive load of 10 Ω was applied. The stator current waveforms were then recorded exclusively under these stable conditions to avoid the inherent fluctuations associated with the transient phase, which typically introduces significant variations in voltage, current, and torque. Figures 18(a)–18(f) illustrate the current, voltage, and torque waveforms under the healthy condition and the case of a single failed capacitive element, presented as two illustrative examples of the signal shape. Higher degradation levels (two to five failed elements) were also simulated; however, their results are not shown here for brevity, as they follow the same progressive distortion trend with increased harmonic content and loss of sinusoidal symmetry.

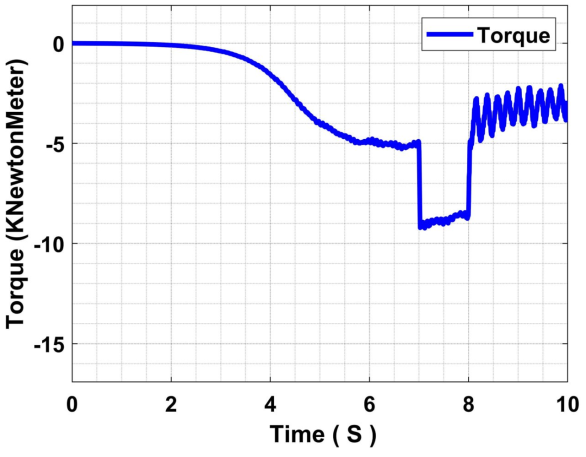

FIG. 17. Torque behavior under open phase fault.

In the current signals shown in Figs. 18(a)–18(f), subtle distortions first appear in phase C. However, in the case of a single failed capacitive element, these distortions are not visually discernible, as the signal largely retains its sinusoidal shape. As the fault progresses, the distortions gradually become more pronounced. The voltage waveforms presented in Figs. 19(a)–19(f) maintain a sinusoidal profile but exhibit slight variations in peak magnitude and balance as degradation increases. The torque profiles in Figs. 20(a)–20(f) display a gradual degradation, where the torque settles at approximately −7 kN m when 5 elements fail, having been stable at −10 kN m in the healthy generator case, indicating a dynamic deterioration. These deviations, often beyond visual discernment, highlight the importance of intelligent diagnostic methods capable of detecting faults at an early stage.

F. Comparative performance analysis of fault classification models

The classification performance was evaluated using several quantitative metrics. Overall accuracy was used as a global indicator of correct predictions. In addition, precision, recall, and F1-score were computed for each class to provide detailed insight into the model's performance. Precision is calculated as $Precision = \frac{TP}{TP+FP}$, recall as

Published under an exclusive license by AIP Publishing

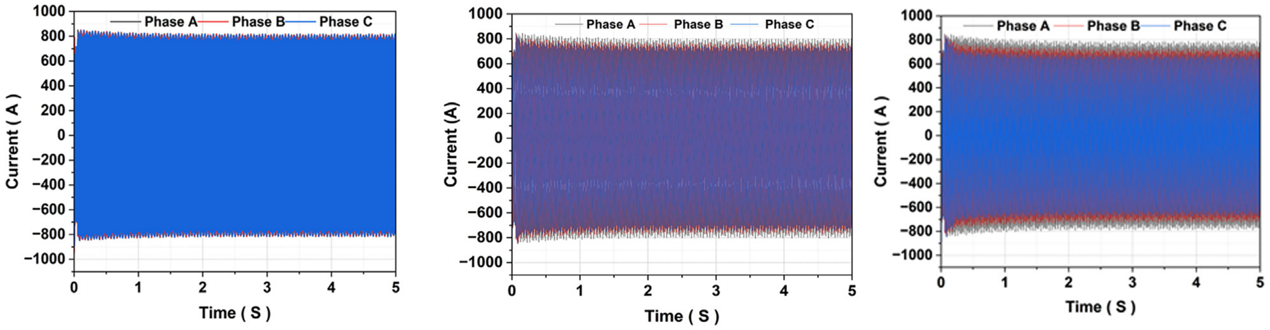

(a) Healthy state (b) One failed element (c) Two elements failed

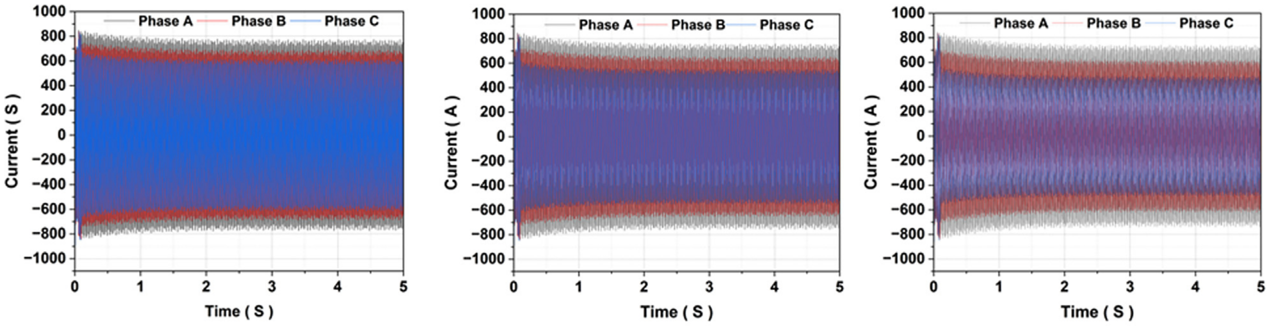

(d) Three elements failed (e) Four elements failed (f) Five elements failed

FIG. 18. Line current under progressive failure of internal capacitive elements: (a) Healthy state, (b) one failed element, (c) two elements failed, (d) three elements failed, (e) four elements failed, and (f) five elements failed.

$Recall = \frac{TP}{TP+FN}$, and F1-score as $F1 - score = \frac{2.Precision.Recall}{Precision+Recall}$, where TP, FP, and FN represent the number of true positives, false positives, and false negatives, respectively. The analysis also included normalized confusion matrices to visualize class-wise prediction accuracy, and receiver operating characteristic (ROC) curves were plotted for each class using one-vs-rest strategy, with AUC values serving as an indicator of separability. Finally, training and prediction times were measured to evaluate the computational efficiency of the models. To ensure robust results, all models were assessed using 10 repeated random hold-out splits (70/30). Figure 21 and Table III summarize the classification accuracy, training time, and prediction time, with Table III additionally reporting the mean accuracy and standard deviation across the splits.

It is evident from Fig. 21 and Table III that the lightweight CNN achieved the highest classification accuracy of 99.91%, with a mean accuracy of 99.80% and a low standard deviation of 0.15%, reflecting very consistent performance across repeated splits. However, this performance necessitated the longest training (557.09 s) and prediction (13.38 s) times, indicating a considerable computational burden. The RF model followed, demonstrating an accuracy of 97.06%, a mean accuracy of 96.80%, and a STD of 0.85%, coupled with moderate training (4.7 s) and prediction (0.71 s) times, benefiting from its ensemble learning strategy. The KNN algorithm yielded an accuracy of 94.12% (mean 93.90%, STD 1.10%) with a significantly short training time (0.37 s), yet its prediction time reached 0.11 s due to its instance-based nature. The SVM achieved 91.18% accuracy, with a mean of 90.95% and STD of 1.50%, characterized by efficient training (0.4 s) and prediction (0.05 s) performance. Although NB recorded the lowest accuracy (88.24%), it demonstrated a mean accuracy of 88% with a STD of 1.90% and the fastest training (0.3046 s) and prediction (0.0830 s) times. With the aim of assessing the classification capability of each model across different fault categories, the confusion matrices presented in Figs. 22(a)–22(e) were generated based on experimental results. These matrices illustrate the distribution of predictions across fault classes, providing insight into each model's diagnostic accuracy. The CNN confusion matrix [Fig. 22(d)] demonstrates that the model exhibits superior classification performance across all classes (F0–F5). These results underscore the model's exceptional generalization ability and its robust capacity to extract highly discriminative features from time-domain signals, even in the presence of closely related fault conditions.

In contrast, the RF model shown in Fig. 22(a) also performed well overall, achieving 100% accuracy in most fault categories. However, it exhibited a notable confusion between F2 and F1, with 17% of F2 samples misclassified as F1. This confusion may be attributed to the similarity in the statistical features extracted from these two classes, which limits the model's ability to draw clear decision boundaries. The KNN classifier shown in Fig. 22(b) achieved generally high accuracy, correctly identifying most classes. However, it exhibited confusion between F4 and F3, and also misclassified a portion of F5

Published under an exclusive license by AIP Publishing

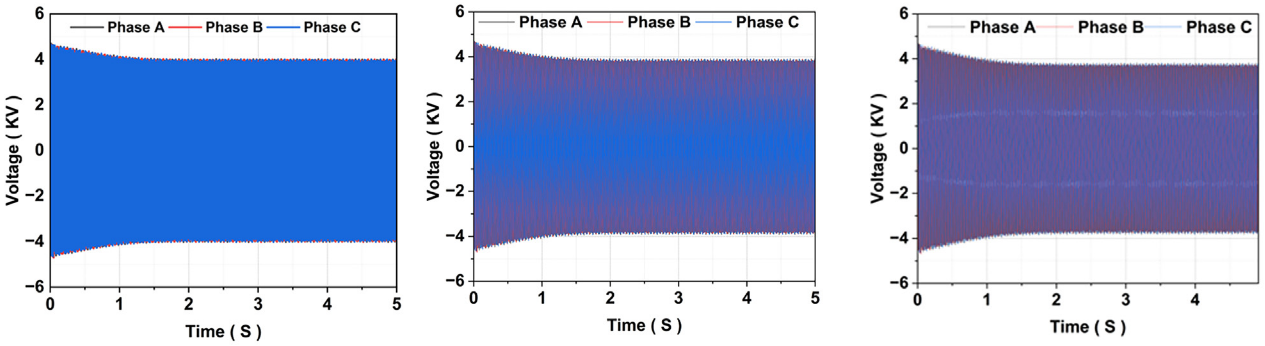

(a) Healthy state (b) One failed element (c) Two elements Failed

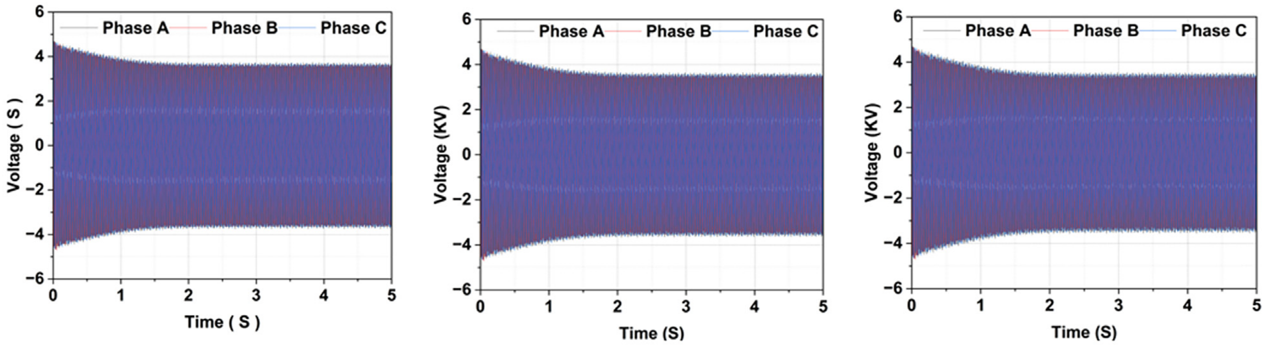

(d) Three elements Failed (e) Four elements failed (f) Five elements failed

FIG. 19. Voltage waveform distortion across fault scenarios: (a) Healthy state, (b) one failed element, (c) two elements failed, (d) three elements failed, (e) four elements failed, and (f) five elements failed.

samples as F2. This suggests overlapping feature distributions in these particular fault categories. The SVM model, shown in Fig. 22(c), demonstrated moderate performance, correctly classifying 67% of the F2 samples, while the rest were misclassified as F1 and F3. This outcome can be attributed to the nature of SVM, which relies on clear margin separation between classes. In this case, the extracted features may not be linearly separable in the transformed feature space, limiting the model's ability to construct effective hyperplanes. As a result, SVM struggles to distinguish between closely spaced or overlapping fault patterns such as F2, F1, and F3.

Finally, the NB classifier, as illustrated in Fig. 22(e), achieved perfect classification for classes F0, F1, and F3. However, it showed noticeable misclassification for classes F2, F4, and F5. This performance degradation can be attributed to the classifier's strong assumption of feature independence, which is unlikely to hold in this context involving complex signal interactions. As a result, its capability to model correlated or nonlinear features is inherently limited. Tables IV–VIII, provide a detailed evaluation of the classification performance of each model using precision, recall, and F1-score metrics across all fault categories. These class-wise metrics offer deeper insight into the strengths and limitations of each classifier beyond overall accuracy. It can be observed that the RF classifier (Table IV) achieved strong and consistent performance, recording perfect precision and recall for most classes. However, slight confusion was noted between fault3 and fault4, leading to an F1-score of 0.91, suggesting partial overlap in the extracted feature space. The KNN (Table V) also demonstrated high classification reliability. It yielded flawless performance for healthy, F1, and F3 classes, while F5 showed a minor drop in recall (0.83). Nevertheless, all F1-scores remained above 0.90, indicating robust overall behavior. In contrast, the SVM classifier (Table VI) exhibited lower class separability, particularly for F2 and F3. The model recorded a reduced recall of 0.67 for fault2 and displayed confusion between overlapping classes, resulting in a lower F1-score of 0.80. The CNN (Table VII) outperformed all other models, achieving F1-scores exceeding 0.99 in every class, with a micro-average of 0.997. This confirms the CNN's superior ability to extract meaningful features and maintain generalization, even in complex and closely related fault conditions. On the other hand, the NB model (Table VIII) showed limitations in handling overlapping fault categories. While it performed perfectly for healthy and F1 classes, it suffered noticeable declines in F2 and F3 most notably a precision score of 0.56 for F3 ultimately resulting in the lowest overall performance among the evaluated models.

To further assess the generalization ability of the models in distinguishing between fault categories, receiver operating

Published under an exclusive license by AIP Publishing

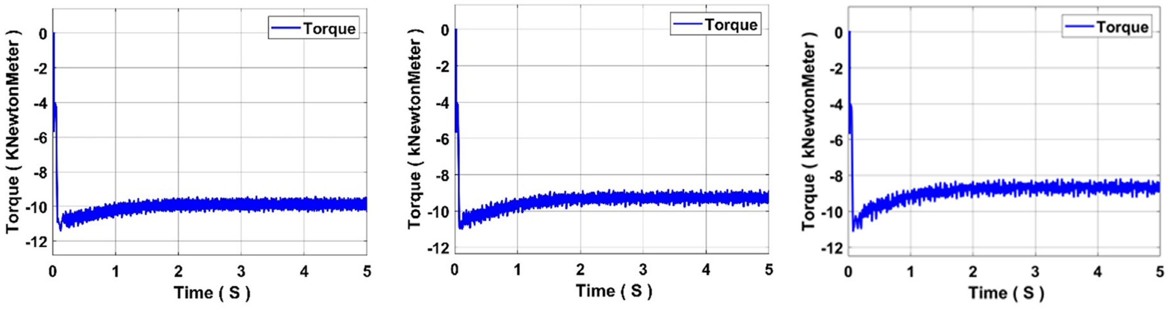

(a) Healthy state (b) One failed element (c) Two elements failed

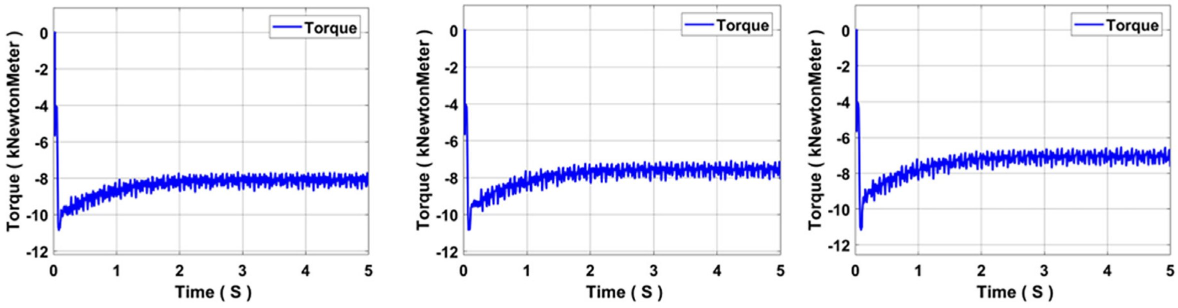

(d) Three elements failed (e) Four elements failed (f) Five elements failed

FIG. 20. Electromagnetic torque distortion across fault scenarios: (a) Healthy state, (b) one failed element, (c) two elements failed, (d) three elements failed, (e) four elements failed, and (f) five elements failed.

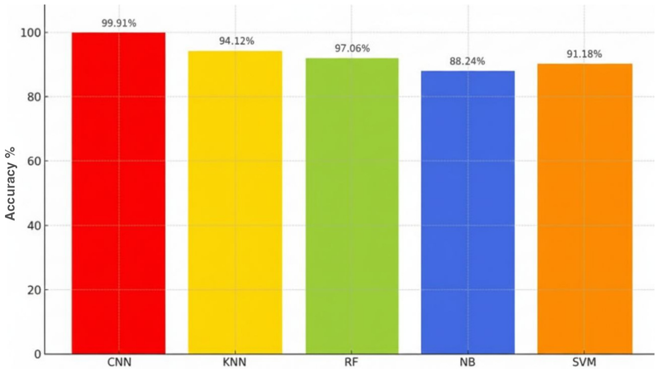

FIG. 21. Comparison of classifier accuracy.

characteristic (ROC) curves were plotted for each classifier, as shown in Figs. 23(a)–23(f). These curves were computed using the one-vs-all strategy on the test dataset, allowing for a detailed evaluation of each model's class-wise discrimination performance. It can be observed that the RF classifier [Fig. 23(a)] achieved high AUC values across most classes, with a slight drop noted for F2 (AUC = 0.89). The KNN model [Fig. 23(b)] also demonstrated strong performance, though its ability to distinguish F5 was slightly reduced (AUC = 0.91).

In Fig. 23(c), the SVM classifier showed inconsistent behavior, particularly in class F2 (AUC = 0.76), reflecting sensitivity to overlapping feature distributions. By contrast, the CNN model [Fig. 23(d)] exhibited outstanding generalization, maintaining near-perfect AUC values ($\geq$0.94) for all classes. As shown in Fig. 23(e), the NB model achieved reasonable results overall, yet

TABLE III. Performance for each classifier.

Model	Prediction time (s)	Training time (s)	Accuracy (%)	Mean accuracy (%)	STD (%)
RF	0.71	4.7	97.06	96.80	0.85
KNN	0.11	0.37	94.12	93.90	1.10
SVM	0.05	0.4	91.18	90.95	1.50
CNN	13.38	557.09	99.91	99.80	0.15
NB	0.0830	0.3046	88.24	88	1.90

Published under an exclusive license by AIP Publishing

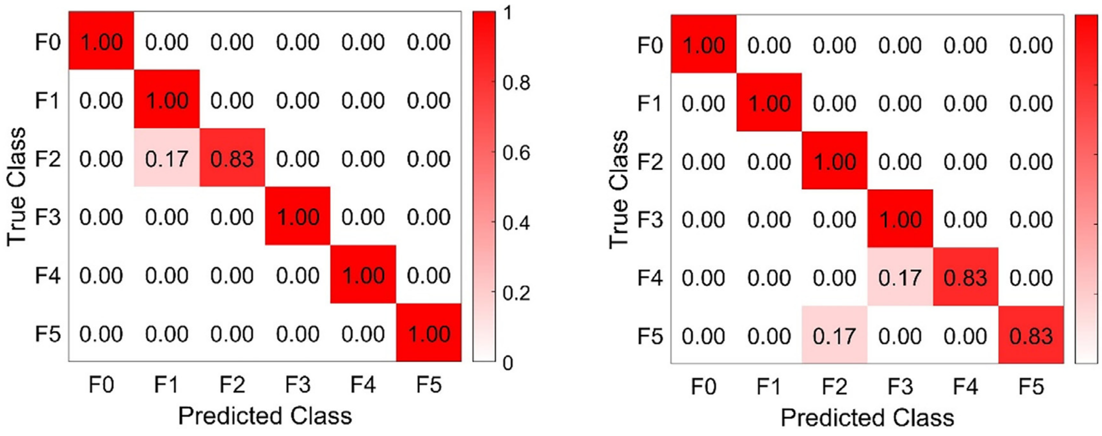

(a) RF Confusion matrices (b) KNN Confusion matrices t

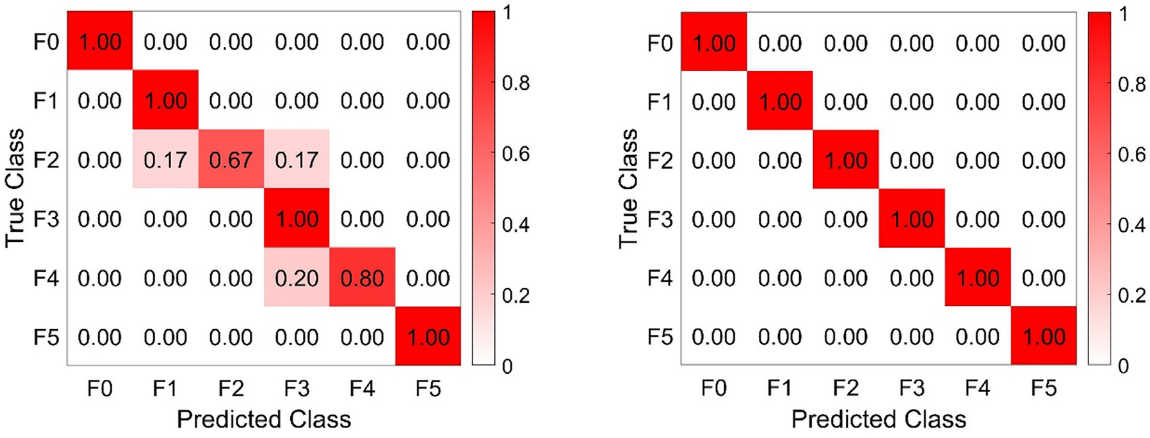

(c) SVM Confusion matrices (d) CNN Confusion matrices

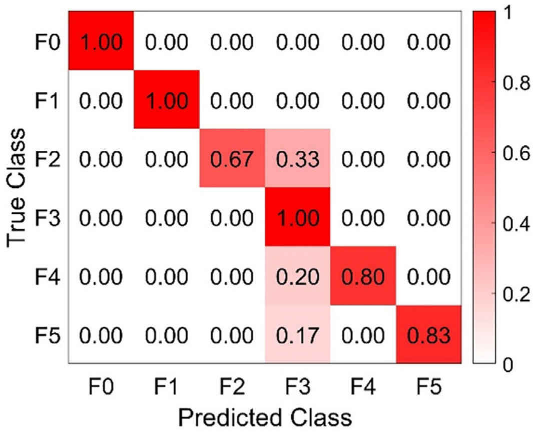

(e) NB Confusion matrices

FIG. 22. Confusion matrices for different classifiers: (a) RF confusion matrices, (b) KNN confusion matrices, (c) SVM confusion matrices, (d) CNN confusion matrices, and (e) NB confusion matrices.

TABLE IV. Performance for RF.

Class	Precision	Recall	F1_score
F0	1	1	1
F1	0.857 14	1	0.923 08
F2	1	0.833 33	0.909 09
F3	1	1	1
F4	1	1	1
F5	1	1	1
Micro-average	0.976	0.972	0.972

TABLE V. Performance for KNN.

Class	Precision	Recall	F1_score
F0	1	1	1
F1	1	1	1
F2	0.833 33	1	0.909 09
F3	0.857 14	1	0.923 08
F4	1	0.833 33	0.909 09
F5	1	0.833 33	0.909 09
Micro-average	0.948	0.944	0.942

TABLE VI. Performance for SVM.

Class	Precision	Recall	F1_score
F0	1	1	1
F1	0.857 14	1	0.923 08
F2	1	0.666 67	0.8
F3	0.75	1	0.857 14
F4	1	0.8	0.888 89
F5	1	1	1
Micro-average	0.934	0.911	0.912

TABLE VII. Performance for CNN.

Class	Precision	Recall	F1_score
F0	1	1	1
F1	1	0.997 19	0.998 59
F2	0.9943	1	0.997 14
F3	1	0.997 19	0.998 59
F4	1	1	1
F5	1	1	1
Micro-average	0.999	0.999	0.999

its performance for F4 dropped to 0.86, likely due to its assumption of feature independence. These findings indicate that CNN and RF are the most reliable classifiers for this application, offering high AUC values and robust generalization across fault types.

TABLE VIII. Performance for NB.

Class	Precision	Recall	F1_score
F0	1	1	1
F1	1	1	1
F2	1	0.666 67	0.8
F3	0.555 56	0.833 33	0.714 29
F4	1	0.8	0.888 89
F5	1	0.833 33	0.909 09
Micro-average	0.926	0.856	0.885

While CNN delivers superior accuracy, RF presents a favorable trade-off between classification performance and computational efficiency. The KNN model remains effective for clearly separated faults, whereas SVM and NB are more vulnerable to performance degradation in the presence of class overlap or complex patterns. This underlines the importance of selecting a classifier that aligns with the data characteristics and practical deployment constraints.

G. Evaluation of CNN model robustness under variable operating conditions

This section evaluates the robustness and generalization capability of the CNN model on unseen datasets. Because of the high sensitivity of the SEIG outputs to speed and mechanical excitation, testing was performed under variable operating conditions where the rotor speed was tightly constrained between 3120 and 3150 rpm. This extremely narrow range, intentionally positioned just above the synchronous speed (3110 rpm), ensures a low-slip environment that adds a critical layer of depth and precision to the evaluation. This setup demonstrates the CNN's efficacy in distinguishing between the most subtle speed variations, thereby confirming its robustness in highly sensitive dynamic environments. Figure 24 illustrates the adopted speed profile.

Figure 25 shows the measured current signal under these variable speed conditions and simultaneous gradual capacitor faults.

Figure 26 shows the measured voltage signal under these variable speed conditions and simultaneous gradual capacitor faults.

Figure 27 shows the measured electromagnetic torque distortion under these variable speed conditions and simultaneous gradual capacitor faults.

Analysis of the signals under varying rotor speed conditions revealed a tangible exacerbation of faults compared to steady-state operation, where voltage signals registered pronounced distortions while current signals exhibited sharp and distinct fluctuations. The most significant impact was observed on the torque signal, which suffered substantial dynamic degradation, confirming the high sensitivity of the SEIG to simultaneous changes in capacitive excitation parameters and rotor speed. This dynamic dataset poses a critical challenge to the robustness of the proposed CNN model, as successful diagnosis necessitates the model's ability to extract fundamental fault features while decoupling them from the variance introduced by varying operating conditions.

Table IX illustrates the performance of the CNN model when applied to the new dataset incorporating varying rotor speed conditions. Despite the complex signal variance, key performance metrics

Published under an exclusive license by AIP Publishing

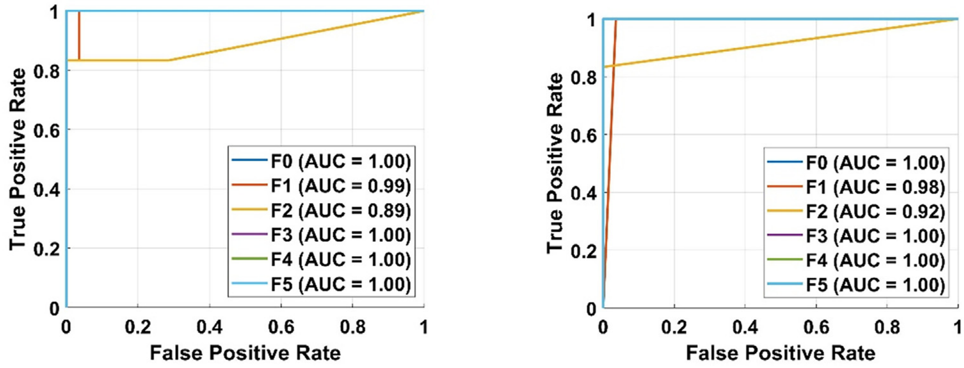

(a) ROC Curve for RF (b) ROC Curve for KNN

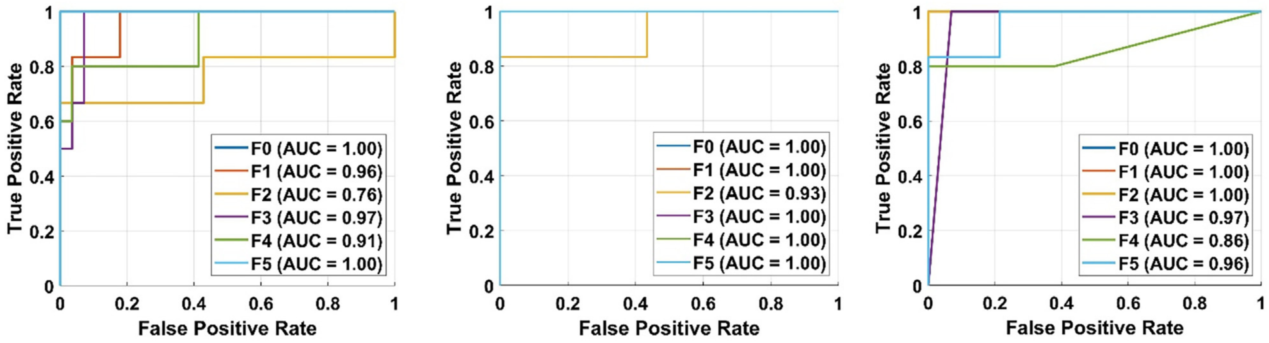

(c) ROC Curve for SVM (d) ROC Curve for CNN (e) ROC Curve for NB

FIG. 23. ROC curves for each classifier: (a) ROC curve for RF, (b) ROC curve for KNN, (c) ROC curve for SVM, (d) ROC curve for CNN, and (e) ROC curve for NB.

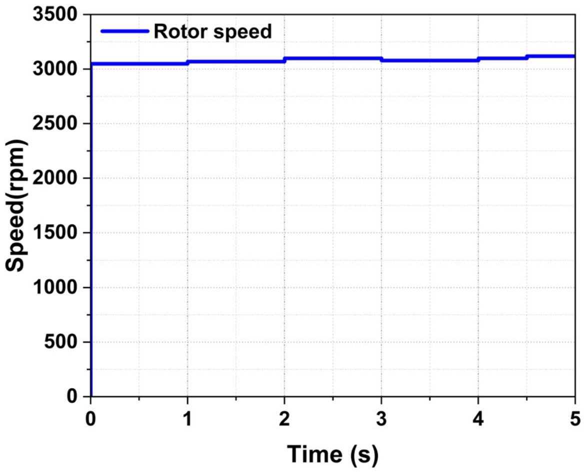

FIG. 24. Rotor speed profile.

such as accuracy, the F1-score, and recall indicate that the model possesses a high level of diagnostic robustness.

To further enhance the performance assessment, the accompanying confusion matrix provides a detailed analysis of the model's ability to discriminate between the various fault classes and healthy operating states, affirming the efficacy of feature extraction within this dynamic environment. Figure 28 presents the confusion matrices demonstrating cnn performance under varying rotor speed conditions.

The superior diagnostic reliability offered by the CNN model is a prerequisite for the robust and safe deployment of the SEIG in MGs, despite the inherent computational trade-off (CNN prediction time: 14.58 s vs RF: 0.7 s). While the RF model offers faster inference, its lower mean accuracy (96.80%) and significantly lower stability STD of 0.85% render it suboptimal for critical applications. In stark contrast, the CNN achieves a near-perfect Mean Accuracy (99.80%) coupled with excellent stability (STD of only 0.15%) on the training data (99.91%). Crucially, the high robustness of the CNN is unequivocally confirmed by its performance on the new, dynamic test data (incorporating varying rotor speed conditions), where it sustained an exceptional Accuracy of 99.67%, providing clear evidence of the model's durability and generalization capability. In high-voltage SEIG fault diagnosis, this high robustness justifies the computational cost. To further reinforce the performance assessment, the confusion matrix demonstrates an exceptional ability to discriminate between classes, where the diagonal band for all fault cases (F0-F5) appears at the maximum value (1.00) with only a minor misclassification in case F2 (by 0.02%). This high performance, further substantiated by the near-unity values of precision, recall, and the F1-score metrics (most of which range

Published under an exclusive license by AIP Publishing

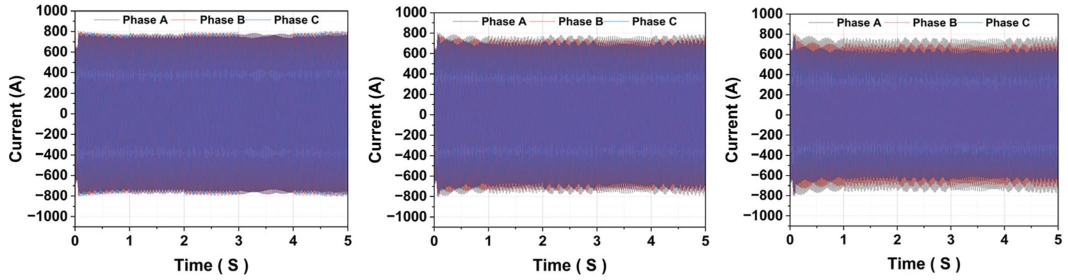

(a) Healthy state (b) One failed element (c) Two elements failed

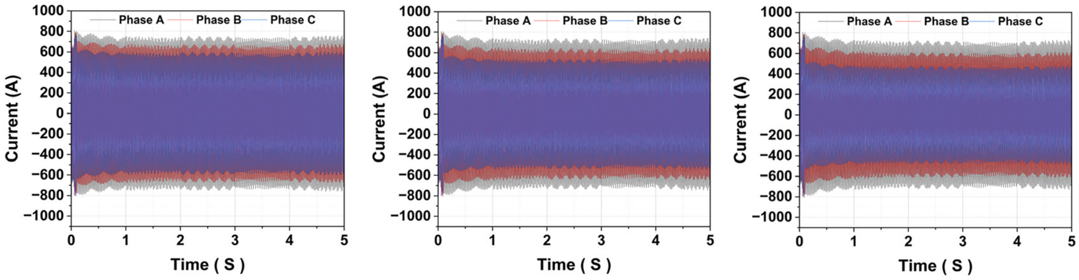

(d) Three elements failed (e) Four elements failed (f) Five elements failed

FIG. 25. Line current under progressive failure of internal capacitive elements at varying rotor speeds: (a) Healthy state, (b) one failed element, (c) two elements failed, (d) three elements failed, (e) four elements failed, and (f) five elements failed.

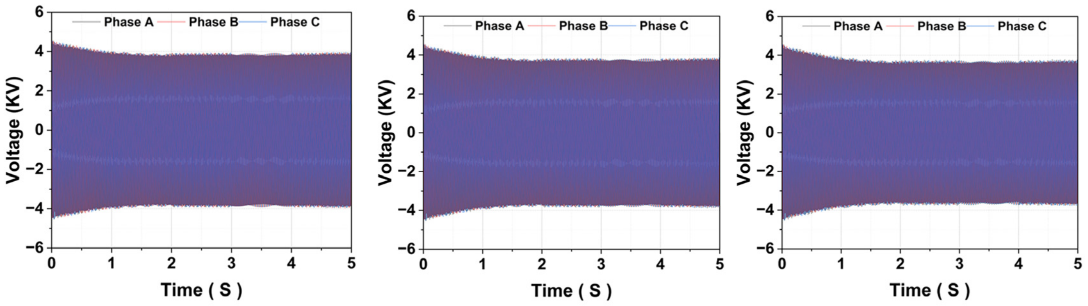

(a) Healthy state (b) One failed element (c) Two elements Failed

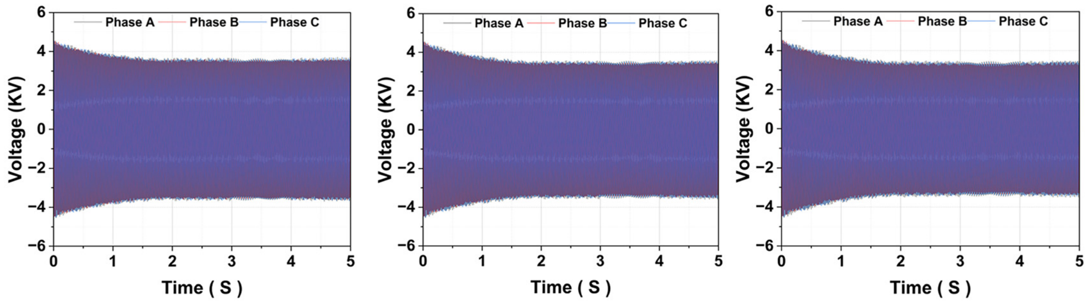

(d) Three elements Failed (e) Four elements failed (f) Five elements failed

FIG. 26. Voltage waveform under progressive failure of internal capacitive elements at varying rotor speeds: (a) Healthy state, (b) one failed element, (c) two elements failed, (d) three elements failed, (e) four elements failed, and (f) five elements failed.

Published under an exclusive license by AIP Publishing

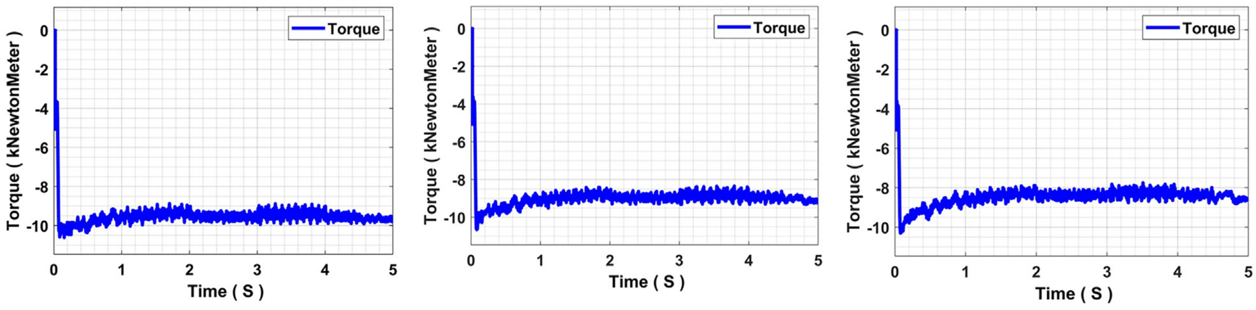

(a) Healthy state (b) One failed element (c) Two elements failed

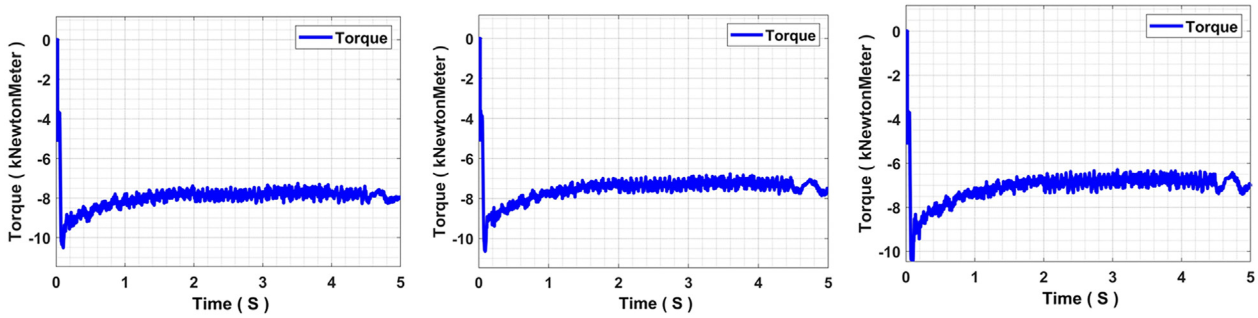

(d) Three elements failed (e) Four elements failed (f) Five elements failed

FIG. 27. Electromagnetic torque under progressive failure of internal capacitive elements at varying rotor speeds: (a) Healthy state, (b) one failed element, (c) two elements failed, (d) three elements failed, (e) four elements failed, and (f) five elements failed.

TABLE IX. Performance of the CNN model applied to dynamic operation data.

Class	Precision	Recall	F1_score
F0	1	0.997 19	0.998 59
F1	0.988 67	1	0.994 3
F2	0.994 4	0.997 19	0.997 19
F3	1	0.988 76	0.994 35
F4	0.997 19	0.997 19	0.997 19
F5	1	1	1
Micro-average	0.996 7	0.996 7	0.996 9

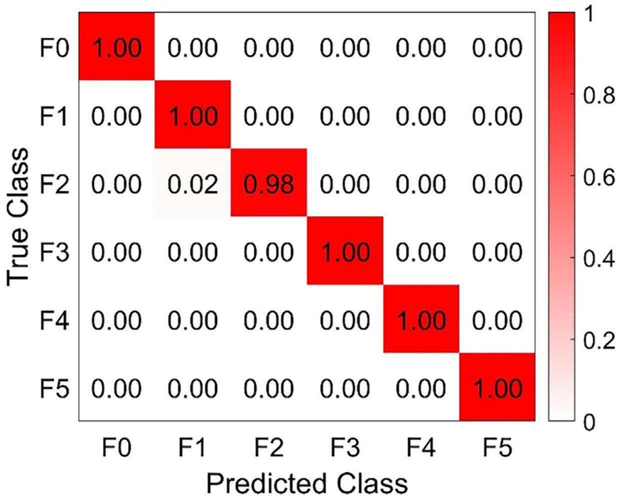

FIG. 28. Confusion matrices demonstrating CNN performance under varying rotor speed conditions.

between 0.9943 and 1.00), proves the model's capacity to extract core fault features and decouple them from the variance induced by speed changes. Therefore, the substantial gain in diagnostic reliability and stability provided by the CNN, even under complex dynamic conditions, thoroughly justifies the investment in computational complexity. Although the model's training time reached 417.22 s and the prediction time was 14.58 s, the current prediction time can be drastically improved by deployment onto dedicated edge hardware (such as field-programmable gate array (FPGA) or tensor processing unit (TPU). This provides a practical and efficient pathway to ensure that the superior performance of the CNN model is effectively utilized for reliable, real-time diagnostic needs with minimal latency. Table X summarizes the key methodologies and reported performance accuracies from previous studies on fault diagnosis and forecasting in wind energy systems and induction machines, as well as the proposed approach in this work.

Published under an exclusive license by AIP Publishing

TABLE X. Comparative analyses of ML- and DL-based fault diagnosis and forecasting methods.

Reference	Methodology	Best accuracy
Dalei and Mohanty[28]	Studied SEIG performance under various electrical faults using the d–q frame model. Fault features were extracted via Hilbert–Huang Transform (HHT) and classified using least squares support vector machine (LS-SVM), then compared with other models (SVM, PNN). Simulations were performed in MATLAB.	99.25% fault classification accuracy with LS-SVM, outperforming the compared models.
Fezai *et al.*[29]	Developed enhanced RF algorithms for wind energy conversion (WEC) fault diagnosis to overcome issues in raw data (noise, redundancy, and variable correlation). The proposed approach reduced training data size, extracted features using Kernel principal component analysis (PCA), and classified selected components with RF.	Achieved an average fault diagnosis accuracy of 91%.
Mansouri *et al.*[27]	Proposed an improved fault diagnosis method for WEC systems using RNN. A reduced model (R-RNN) combined with H-K-means was developed to lower computational cost, along with two interval-valued models [interval reduced RNN-based centers and ranges (IR-RNNCR), interval reduced RNN-based upper and lower bounds (IR-RNNUL)] to handle noise and uncertainty. The models were implemented and simulated in MATLAB.	98.99% classification accuracy with IR-RNNUL, and 63% reduction in computation time.
Skowron *et al.*[30]	The paper presents the idea of using a CNN for the diagnosis and detection of incipient stator inter-turn short-circuit (ITSC) faults in an inverter-fed Induction Motor (IM).	The highest accuracy achieved by the proposed model is 99.3%.
Skowron and Orłowska-Kowalska.[31]	This study introduces a fault diagnosis method for an inverter-fed Induction Motor (IM) using Cascaded Neural Networks (CdNN), specifically combining structures like self-organizing map multilayer perceptron (SOM-MLP) and self-organizing map recurrent hidden network (SOM-RHN).	The highest accuracy achieved by the proposed model is 99.6%.
Mejia-Barron *et al.*[32]	The paper presents a model based on a Multilayer Neural Network (MLNN) to simulate the current signatures of an Induction Motor (IM) under Inter-Turn Short-Circuit (ITSC) stator faults.	The highest accuracy achieved by the proposed model is 80%–92%.
Rajamany *et al.*[33]	This study addresses an online diagnostic methodology for Stator Inter-Turn Short-Circuit (ITSC) faults in Induction Motors (IMs) by integrating sequence components with an Artificial Neural Network (ANN).	The highest accuracy achieved by the proposed model is 99.6%.
This work	This study proposes an innovative diagnostic framework for SEIGs under healthy and faulty conditions, utilizing the FEM to model the machine and analyze the current, voltage, and torque responses to capture fault characteristics; FFT was applied to detect anomalies under balanced and unbalanced loads, focusing on progressive capacitor degradation. The diagnostic approach utilized advanced signal processing to extract a comprehensive set of features, including Time-domain features (such as ZCR, RMS, STD, mean, energy, PTP amplitude, and crest factor), statistical descriptors (Kurtosis, Skewness), spectral features derived from FFT (spectral centroid, entropy, flatness, and band power), Hjorth parameters (activity, mobility, and complexity), and autocorrelation coefficients at lags 1 and 2, which collectively characterize the signal's properties. A hybrid approach combining FEM-based modeling and intelligent algorithms (including ML algorithms like RF, NB, SVM, and KNN, alongside the DL model CNN) achieved accurate fault classification, highlighting the framework's potential as an intelligent tool for predictive maintenance in standalone wind energy systems.	The CNN model achieved the highest classification accuracy of 99.91%, followed by 97.06% for the RF model.

IX. CONCLUSION

This paper introduces a holistic hybrid diagnostic framework that merges high-resolution finite-element modeling, time–frequency signal processing, and both machine-learning and deep-learning classifiers to enhance the reliability of the SEIGs in wind-energy MGs. The TSFEM succeeded in capturing the electromagnetic behavior of a 4.087 MW SEIG with unprecedented physical resolution. The proposed work has successfully simulated several faulty scenarios, such as healthy, unbalanced load, open phase, and progressive capacitor degradation. Again, the collective use of time-domain, spectral, and statistical features with ML classifiers showed strong diagnostic potential. The proposed lightweight CNN trained on wavelet scalograms

Published under an exclusive license by AIP Publishing

demonstrated exceptional performance with 99.91% accuracy, F1-scores above 0.99, and an AUC of more than 0.98, outperforming RF, KNN, SVM, and NB by 2.85%–13.12%. These results confirm that merging physics-based modeling with data-driven intelligence provides a powerful and scalable solution for early fault detection, predictive maintenance, and long-term operational stability in isolated renewable-energy systems. Building on the promising test results of this work, several future research directions are envisaged: (i) a hardware in the loop (HIL) real-time implementation will be developed to validate the proposed framework under realistic operating conditions, allowing for online monitoring and rapid decision-making, (ii) the diagnostic system will be further developed into a hybrid FEM-ML digital-twin architecture that will continuously adapt the model from real sensor data, enhancing its robustness against environmental variations, and (iii) the methodology will be expanded into other fault types, including bearing defects, rotor bar failures, eccentricity, and converter-related disturbances. Lightweight embedded-artificial intelligence (AI) versions of the CNN will be optimized for edge deployment inside wind-turbine controllers or MG energy-management units. These will further advance the practical deployment of intelligent, predictive, and self-adaptive monitoring systems for next-generation wind-energy MGs.

AUTHOR DECLARATIONS

Conflict of Interest

The authors have no conflicts to disclose.

Author Contributions

Ali Dilmi: Conceptualization (equal); Formal analysis (equal); Investigation (equal); Methodology (equal); Writing – original draft (equal). **Ahcene Bouzida:** Methodology (equal); Resources (equal); Software (equal); Validation (equal); Writing – review & editing (equal). **Nacera Yassa:** Data curation (equal); Investigation (equal); Resources (equal); Visualization (equal); Writing – review & editing (equal). **Belynda Fares:** Formal analysis (equal); Software (equal); Visualization (equal). **Riyadh Bouddou:** Conceptualization (equal); Methodology (equal); Project administration (equal); Supervision (equal); Validation (equal); Writing – review & editing (equal). **Ayodeji Olalekan Salau:** Formal analysis (equal); Funding acquisition (equal); Resources (equal); Writing – review & editing (equal).

DATA AVAILABILITY

The data that support the findings of this study are available from the corresponding author upon reasonable request.

REFERENCES

[1] S. Shahzad, M. A. Abbasi, H. Ali, M. Iqbal, R. Munir, and H. Kilic, "Possibilities, challenges, and future opportunities of microgrids: A review," Sustainability **15**(8), 6366 (2023).

[2] M. A. Bekhti, L. Ghomri, H. L. Beklaouz, and R. Bouddou, "Techno-economic and environmental optimization of standalone hybrid energy systems using advanced energy storage for remote electrification in Southern Algeria," J. Renewable Sustainable Energy **17**(5), 056309 (2025).

[3] V. M. Krishna, V. Sandeep, S. S. Murthy, and K. Yadlapati, "Experimental investigation on performance comparison of self-excited induction generator and permanent magnet synchronous generator for small-scale renewable energy applications," Renewable Energy **195**, 431–441 (2022).

[4] A. Mseddi, B. Dhouib, M. A. Zdiri, Z. Alaas, O. Naifar, T. Guesmi, B. M. Alshammari, and K. Alqunun, "Exploring the potential of hybrid excitation synchronous generators in wind energy: A comprehensive analysis and overview," Processes **12**(6), 1186 (2024).

[5] A. Roy and S. Bandyopadhyay, *Wind Power Based Isolated Energy Systems* (Springer International Publishing, Cham, 2019).

[6] M. I. Abuashour, O. Tha'er, A. Al-Kurdi, and M. Al-Maaitah, "Automatic reactive power compensation utilizing variable excitation capacitance for wind turbine employing SEIG for feeding IM driving centrifugal pump," Int. J. Latest Res. Sci. Technol. **3**(3), 19–28 (2020).

[7] K. Laadjal and A. J. M. Cardoso, "Multilayer ceramic capacitors: An overview of failure mechanisms, perspectives, and challenges," Electronics **12**(6), 1297 (2023).

[8] W. Liu, X. Sun, X. Yan, Y. Gao, X. Zhang, K. Wang, and Y. Ma, "Review of energy storage capacitor technology," Batteries **10**(8), 271 (2024).

[9] A. Achar, Y. Djeriri, H. Benbouhenni, R. Bouddou, and Z. M. S. Elbarbary, "Modified vector-controlled DFIG wind energy system using robust model predictive rotor current control," Arab. J. Sci. Eng. **50**(14), 11065–11089 (2025).

[10] S. Kundu, "Improved dynamic performance of SEIG-based wind energy systems for off-grid applications," Electr. Power Syst. Res. **251**, 112198 (2026).

[11] M. R. I. Tomal, A. Kabir, M. Hasan, S. M. Haque, and M. M. H. Jony, "Energy: A comprehensive review," in *Machine Learning Technologies on Energy Economics and Finance: Energy Sustainable Analytics* (Springer, 2025), Vol. 1, pp. 367.

[12] C. S. Mahinay, C. Reyes, R. Calanog *et al.*, "Intricacies in the failure analysis of integrated capacitors," J. Fail. Anal. Prev. **24**, 2058–2073 (2024).

[13] R. Kalbitz, "Evaluation and modeling of long-term endurance measurement on electric double layer capacitors to increase reliability of lifetime predictions," Intell. Sustainable Manuf. **2**(2), 10023 (2025).

[14] A. Pena-Quintal, U. Mustafa, C. Gerada, and M. R. Ahmed, "On accelerated degradation of DC-link film capacitors and data-based lifetime estimation," IEEE Access. **12**, 177565 (2024).

[15] S. Akbar, T. Vaimann, B. Asad, A. Kallaste, M. U. Sardar, and K. Kudelina, "State-of-the-art techniques for fault diagnosis in electrical machines: Advancements and future directions," Energies **16**(17), 6345 (2023).

[16] J. Yu and Y. Zhang, "Challenges and opportunities of deep learning-based process fault detection and diagnosis: A review," Neural Comput. Appl. **35**(1), 211–252 (2023).

[17] T. T. Khoei, H. O. Slimane, and N. Kaabouch, "Deep learning: Systematic review, models, challenges, and research directions," Neural Comput. Appl. **35**(31), 23103–23124 (2023).

[18] M. K. Rajak, J. Samanta, and R. Pudur, "A hardware-based novel approach for parallel operation of two differently rated SEIGs," Results Eng. **17**, 100825 (2023).

[19] H. Liu, Y. Wang, T. Zeng, H. Wang, S. C. Chan, and L. Ran, "Wind turbine generator failure analysis and fault diagnosis: A review," IET Renewable Power Gener. **18**(15), 3127–3148 (2024).

[20] J. Barzola and J. Chandi, "Magnetic field simulation and torque–speed performance of a single-phase squirrel-cage induction motor: An FEM and experimental approach," Machines **13**(6), 492 (2025).

[21] A. Bouzida, R. Abdelli, O. Touhami, and A. Aibeche, "Dynamic eccentricity fault diagnosis in induction motors using finite element method and experimental tests," Int. J. Ind. Electron. Drives **3**(4), 199–209 (2017).

[22] V. B. M. Krishna, S. S. S. R. S. Duvvuri, P. V. S. Sobhan, K. Yadlapati, V. Sandeep, and B. K. Narendra, "Experimental study on excitation phenomena of renewable-energy-source-driven induction generator for isolated rural community loads," Results Eng. **21**, 101761 (2024).

[23] H. Zhang, H. Tan, and M. A. Marwat, "Applications and prospects of dielectric materials for capacitive energy storage," in *Dielectric Materials for Capacitive Energy Storage* (CRC Press, 2024), pp. 166–204.

[24] B. Du and M. Xiao, "Polypropylene film," in *Polypropylene Film for HVDC Capacitors* (Springer Nature Singapore, Singapore, 2025), pp. 19–48.

[25] J. L. Bermudez and S. Nilsson, "Capacitors for LCC and VSC HVDC converter stations," in *High Voltage DC Transmission Systems*, CIGRE Green Books, edited by B. R. Andersen and S. L. Nilsson (Springer, Cham, 2025).

[26] A. Gupta, O. P. Yadav, D. DeVoto, and J. Major, "A review of degradation behavior and modeling of capacitors," in *Proceedings of the ASME 2018*

Published under an exclusive license by AIP Publishing

International Technical Conference and Exhibition on Packaging and Integration of Electronic and Photonic Microsystems (ASME, San Francisco, CA, 2018), Paper No. V001T04A004.
[27] M. Mansouri, K. Dhibi, M. Hajji, K. Bouzara, H. Nounou, and M. Nounou, "Interval-valued reduced RNN for fault detection and diagnosis in wind energy conversion systems," IEEE Sens. J. **22**(13), 13581–13588 (2022).
[28] J. Dalei and K. B. Mohanty, "Fault classification in SEIG system using Hilbert–Huang transform and least square support vector machine," Int. J. Electr. Power Energy Syst. **76**, 11–22 (2016).
[29] R. Fezai *et al.*, "Effective random forest-based fault detection and diagnosis for wind energy conversion systems," IEEE Sens. J. **21**(5), 6914–6921 (2021).
[30] M. Skowron, T. Orlowska-Kowalska, M. Wolkiewicz, and C. T. Kowalski, "Convolutional neural network-based stator current data-driven incipient stator fault diagnosis of inverter-fed induction motor," Energies **13**(6), 1475 (2020).
[31] M. Skowron and T. Orłowska-Kowalska, "Efficiency of cascaded neural networks in detecting initial damage to induction motor electric windings," Electronics **9**(8), 1314 (2020).
[32] A. Mejia-Barron, G. Tapia-Tinoco, J. R. Razo-Hernandez, M. Valtierra-Rodriguez, and D. Granados-Lieberman, "A neural network-based model for MCSA of inter-turn short-circuit faults in induction motors and its power hardware-in-the-loop simulation," Comput. Electr. Eng. **93**, 107234 (2021).
[33] G. Rajamany, S. Srinivasan, K. Rajamany, and R. K. Natarajan, "Induction motor stator interturn short-circuit fault detection in accordance with line current sequence components using artificial neural network," J. Electr. Comput. Eng. **2019**, 4825787.

Published under an exclusive license by AIP Publishing